Relationships between olivine LPO and deformation parameters in naturally deformed rocks and implications for mantle seismic anisotropy

Rachel E. Bernard[1*], Whitney M. Behr[1†], Thorsten W. Becker[1,2], and David J. Young[3]

[1]Department of Geological Sciences, Jackson School of Geosciences, The University of Texas at Austin, Austin, TX

[2]Institute for Geophysics, Jackson School of Geosciences, The University of Texas at Austin, Austin, TX

[3]School of Earth Sciences, The Ohio State University, Columbus, OH

Key Points:

- Natural samples reveal complex relationships between olivine LPO and deformation conditions
- Olivine LPO varies more often with strain geometry than water and stress in studied peridotites
- B-type olivine LPO can form at low stresses and water contents, plus a wide range of temperatures

*Now at Scripps Institution of Oceanography, University of California San Diego, La Jolla, CA

†Now at Geological Institute, Department of Earth Sciences, Swiss Federal Institute of Technology (ETH), Zurich, Switzerland

Corresponding author: Rachel E. Bernard, `rebernard@ucsd.edu`

Abstract

We analyze peridotites from a wide range of tectonic settings to investigate relationships between olivine lattice preferred orientation (LPO) and deformation conditions in naturally deformed rocks. These samples preserve the five olivine LPO types (A through E-type) that rock deformation experiments have suggested are controlled by water content, temperature, stress magnitude, and pressure. The naturally deformed specimens newly investigated here (65 samples) and compiled from an extensive literature review (445 samples) reveal that these factors may matter less than deformation history and/or geometry. Some trends support those predicted by experimentally determined parametric dependence, but several observations disagree — namely that *all* LPO types are able to form at very low water contents and stresses, and that there is no clear relationship between water content and LPO type. This implies that at the low stresses typical of the mantle, LPO type more often varies as a function of strain geometry. Because olivine LPO is primarily responsible for seismic anisotropy in the upper mantle, the results of this study have several implications. These include (1) the many olivine LPO types recorded in samples from individual localities may explain some of the complex seismic anisotropy patterns observed in the continental mantle, and (2) B-type LPO – where olivine's "fast axes" align perpendicular to flow direction – occurs under many more conditions than traditionally thought. This study highlights the need for more experiments, and the difficulty in using olivine LPO in naturally-deformed peridotites to infer deformation conditions.

1 Introduction

Seismic anisotropy in the upper mantle is produced primarily by lattice-preferred orientation (LPO) developed in olivine during ductile deformation by the common mechanism of dislocation creep (Nicolas & Christensen, 1987). The manner in which olivine's principal axes – [100], [010], and [001] – align with respect to shear direction is often categorized by LPO "types." These types are commonly referred to as A-, B-, C-, D-, and E-type (cf. Karato et al., 2008). A-type, the most frequently occurring configuration, describes an LPO pattern where olivine's [100] axes align in the shear direction, [010] axes align normal to the shear plane, and [001] axes align within the shear plane but normal to the shear direction (Figure 1). Because of the frequent occurrence of this type – and because seismic waves travel fastest along olivine's [100] plane – it is typically assumed that in the earth's mantle, seismic fast directions are oriented in the direction of shear. Seismic anisotropy is one of the

principal means of characterizing upper mantle flow directions, so it is critical to understand how and why these LPO types form, particularly for those types that contradict such an assumption.

The patterns, or morphologies, of olivine LPOs – schematically represented in Figure 1 – are often assumed to reflect the activation of one or more specific slip systems: [100](010) for A-type, [001](010) for B-type, [001](100) for C-type, [100](001) for E-type. D-type is expected when [100](010) and [100](001) are of similar strength. These slip systems are activated as a function of their orientation with respect to applied stress, and their Peierls stress or "yield strength," which can be affected by the physical conditions of deformation (e.g. Mackwell et al., 1985; Bai et al., 1991; Kaminski, 2002). Numerical modeling efforts have demonstrated that most LPO types can be reproduced by varying both "strain geometry" (orientation and magnitude of the principal strain axes with respect to the deformation plane) and slip system strengths (Ribe & Yu, 1991; Wenk et al., 1991; Tommasi et al., 1999, 2000; Kaminski, 2002; Becker et al., 2008). In recent decades, several experiments have focused on the relationship between LPO types and physical deformation conditions, most notably temperature, water content, and deviatoric stress magnitude (e.g. Jung & Karato, 2001; Katayama et al., 2004; Jung et al., 2006; Katayama & Karato, 2006; Ohuchi et al., 2012; Wang et al., 2019). These high temperature and pressure experiments found that at experimental conditions, the less common B- through E-type LPOs form when water contents and/or deviatoric stress magnitudes are elevated relative to conditions resulting in A-type LPO (Figure 1). Several additional recent studies, however, have shown that factors other than water and stress – such as temperature, pressure, deformation mechanism, deformation history, deformation geometry, strain magnitude, and/or the presence of melt – can also affect slip system strength and/or contribute to the development of olivine LPO (e.g. Katayama & Karato, 2006; Sundberg & Cooper, 2008; Jung et al., 2009b; Boneh & Skemer, 2014; Hansen et al., 2014; Précigout & Hirth, 2014; Qi et al., 2018). B-type, for example, has been suggested to form under high pressures, lower temperatures, and/or during grain boundary sliding in some experiments (Katayama & Karato, 2006; Sundberg & Cooper, 2008; Précigout & Hirth, 2014). Other examples include AG-type (also known as axial-010 or "a-c switch") – a sixth LPO type suggested to form in the presence of melt (Holtzman et al., 2003; Qi et al., 2018) – and D-type, which Hansen et al. (2014) demonstrated can develop during dislocation-accommodated grain boundary sliding at lower strains than A-type LPO.

By comparison with experiments, natural peridotites are deformed at orders of magnitude lower strain rates and under a wider range of temperatures, pressures, deviatoric stresses and strain magnitudes than is currently accessible in experiments. Additionally, experiments are conducted (with few exceptions) on initially undeformed samples or synthetic olivine aggregates that generally lack any pre-existing textures or LPOs; whereas in most geologic settings, the lithospheric mantle has experienced multiple phases of deformation, and recent studies indicate that past deformation history is not easily erased, with even completely annealed samples preserving strong LPOs (e.g. Webber et al., 2010; Boneh et al., 2017). Our aim in this paper is to examine LPO development in rocks from natural settings that have likely experienced multiple phases of deformation and highly variable degrees of finite strain. To do this, we use 65 naturally deformed peridotite samples from xenoliths, continental mantle massifs, and ophiolites to explore any trends between deformation conditions and olivine LPO in natural peridotites. Our results are presented alongside samples compiled from 48 previously published studies in which olivine LPOs were measured. We compare our natural dataset to existing experimental constraints, discuss similarities and differences between these two dataset types, and explore implications for seismic anisotropy in the mantle.

2 Sample Descriptions

65 peridotites were newly analyzed for this study (Figure 2 and Tables 1 and 2). 42 are xenoliths from the western US: 7 from the Rio Grande Rift region (2 from Elephant Butte, 2 from Cerro Chato, and 3 from Cerro de Guadalupe); 6 from San Carlos Volcanic Field in Arizona; 3 from Kilbourne Hole in New Mexico; 11 from Lunar Crater Volcanic Field; 15 from the Mojave (7 from Cima Volcanic Field and 8 from Dish Hill). An additional 5 samples derive from the Navajo Volcanic Field in the four corners region of the western US, and are diatreme-hosted inclusions rather than xenoliths. The remaining 6 xenoliths – 5 from the San Quintin Volcanic Field in Mexico and 1 from Eifel Germany – come from outside of the western US. 10 peridotites come from continental massifs: 2 are from the Ivrea Zone in Italy and 8 are from the Bjørkedalen Peridotite in western Norway. The last 2 peridotites come from the Bay of Islands Ophiolite Complex in western Newfoundland. Additional details on these localities can be found in Supplementary Material Text S5.

Most xenolith specimens are spinel lherzolites, wehrlites, and harzburgites (Table 1). Exceptions include some from Lunar Crater that are dunites, and samples from Norway that

contain primarily olivine and tremolite with small amounts of anthophyllite, orthopyroxene, clinopyroxene and spinel. These samples, and some from the Navajo locality that contain chlorite and antigorite, are the only ones that contain hydrous minerals stable under mantle conditions. The peridotites from Newfoundland are the only samples that appear to have been altered significantly through late-stage serpentinization. None of the newly studied peridotites herein contain garnet.

Textures in the samples range from granular to protogranular to porphyroclastic to mylonitic. Granular samples are characterized by large grains (> 2 mm) with abundant triple junctions, no foliation, and only very minor subgrain development in olivine. Protogranular samples have moderately large grains (1–2 mm) and show weak grain elongation with occasional evidence of internal grain deformation. Porphyroclastic samples exhibit large, elongate olivine and orthopyroxene porphyroclasts with irregular grain boundaries and substantial dynamic recrystallization. Mylonitic samples have pervasive dynamic recrystallization, finer grain sizes, and exhibit strong foliations with porphyroclasts that are smaller and significantly more elongate than those in the porphyroclastic category.

Most porphyroclastic to mylonitic samples preserve evidence of deformation via dislocation creep as indicated by 1) internal lattice deformation (e.g., subgrains and undulose extinction); 2) "core-and-mantle" microstructures in which elongate porphyroclasts are surrounded by smaller, equant, dynamically recrystallized grains lacking in internal deformation. An exception are some dunite samples from Norway that show evidence for dislocation-accommodated grain boundary sliding, such as 4-grain junctions, straight grain boundaries parallel to foliation, shape preferred orientation, relatively weak LPO, and minimal internal deformation (e.g. White, 1977). Additional descriptions and images of these microstructures can be found in Supplementary Material Text S6 and Figures S7 and S8.

Deformation temperatures for all samples were estimated based on previously published work, which reported temperatures to varying precision. The inferred temperatures, and other information on these samples, can be found in Tables 1 and 2.

3 Methods

A range of microanalytical techniques were applied to characterize olivine LPO and deformation conditions, as follows.

3.1 SIMS

We used the Cameca 6f Secondary Ion Mass Spectrometer (SIMS) at Arizona State University to measure water concentrations in olivine, orthopyroxene and clinopyroxene, collecting data from 7 mounts over three sessions. In addition to unknowns of every phase, each mount contained some of several olivine, clinopyroxene, and orthopyroxene standards: PMR53, CITI7210, GRR2334a, GRR16506 (Bell et al., 1995; Aubaud et al., 2007; Mosenfelder et al., 2011; Mosenfelder & Rossman, 2013a,b) along with a well-established synthetic forsterite blank (GRR1017, 0 ppm H_2O) (Bell et al., 1995; Mosenfelder & Rossman, 2013a,b) or San Carlos olivine grains with known water content of < 3 ppm H_2O (Marshall et al., 2018). Additional information on sample preparation, applied blank corrections, calibration curves used ($R^2 = 0.89 - 0.98$), and reported standard errors can be found in the Supplementary Material (Text S1, Tables S1 and S2, and Figure S1). Due to the well-documented diffusion of hydrogen in olivine grains during xenolith ascent (e.g. Demouchy et al., 2006; Peslier & Luhr, 2006), *in-situ* (i.e., mantle) olivine water contents are often calculated from partition coefficients applied to measured pyroxene water contents ($D_{opx/ol} = 0.11$ and $D_{cpx/ol} = 0.07$) (e.g. Warren & Hauri, 2014). If water contents were measured for both orthopyroxene and clinopyroxene, the calculated olivine water content was estimated by taking the average value calculated from each mineral.

3.2 X-ray CT

The Xradia microXCT 400 at UT Austin was used to isolate spinel — distinguishable from other phases in scans due to its relatively high density — to identify foliation and lineation in samples where this was not easily recognizable in hand sample, and to quantify the shape preferred orientation (SPO) of spinel grains with implications for strain geometry. FEI Avizo 8.0 software was used to create 3D volume renderings and visualizations (Supplementary Material Text S2 and Figure S2). Quant3D Software was used to quantify the degree of SPO anisotropy and shape of spinel grains through the calculation of fabric tensor eigenvalues (Ketcham & Ryan, 2004) (Supplementary Material Text S2 and Table S3), which in turn were used to calculate the following: P', a parameter that ranges from 1 to infinity and increases with greater anisotropy (Jelinek, 1981), and T, a shape factor ranging from -1 to 1, where negative and positive values indicate prolate and oblate ellipsoids, respectively (Hossack, 1968).

3.3 Grain Size Measurements and Stress Magnitudes

Olivine aspect ratios, subgrain widths, and dynamically recrystallized grain sizes were measured using Zeiss Zen Pro software connected to a Zeiss Axio Imager M2m petrographic microscope. Measurements were averaged for at least 100 dynamically recrystallized grains or subgrains per sample. Prior work has demonstrated that this method yields virtually identical results compared to the linear intercept method conducted optically or using EBSD data (Bernard & Behr, 2017). Average recrystallized grain sizes, after applying a correction factor of 1.2 to account for 2D sectioning, were used to estimate deviatoric stress magnitudes during deformation based on the paleopiezometer of Van der Wal et al. (1993). Olivine aspect ratios in 2-D were used to calculate the constant, k, which defines the slope of a Flinn diagram and describes the shape of a strain ellipsoid as having experienced flattening ($0 < k < 1$, i.e., oblate shapes), plane strain ($k = 1$) or constriction ($k > 1$, i.e., prolate shapes) (Table 2) (Flinn, 1965).

3.4 Electron Backscatter Diffraction (EBSD)

LPO in olivine was measured from polished thin sections with an Oxford EBSD detector installed in the Phillips/FEI XL30 Environmental SEM at The University of Texas at Austin using a 20–25 kV accelerating voltage, 15–20 mm working distance, 30–40X magnification, and 10–50 micron step sizes. Large Area Maps were acquired using Oxford Instruments AZtec software (version 2.1), and post-processing was conducted using MTEX 4.4.0 toolboxes and included noise reduction with a smoothing spline filter (Bachmann et al., 2010). MTEX was also used to estimate modal percentages, make lower hemisphere projection pole figures plotted as one-point-per-grain, to calculate fabric strengths using the M- (Skemer et al., 2005) and J-indices (Bunge, 1982), and to calculate two LPO orientation indices: the BA-index, which quantifies LPOs from zero to 1 where zero represents D-type LPO and 1 represents AG-type LPO, and the Fabric Index Angle (FIA-index), which allows an LPO to be expressed as a single angle (Mainprice et al., 2015; Michibayashi et al., 2016) (see Supplementary Material Table S5).

4 Inclusion and Treatment of Previously Published Data

In addition to measurements on our own samples, we compiled data from a literature review. Data come from 48 studies published in the past 15 years, yielding 445 individual

peridotite samples (see Appendix A and Supplementary Material Text S3 and Table S4 for a list of studies and breakdown of which studies have particular LPO types and analyses). The vast majority of these peridotites are xenoliths and samples from continental massifs; 11 samples come from ophiolitic settings and 4 samples come from one abyssal locality (Figures 2 and 3). The treatment of this previously published data was not always straightforward, particularly when it came to including data for stress, deformation temperature, and water content. In particular, a comparison of water contents involves the non-trivial task of comparing data obtained from olivines and pyroxenes, using SIMS and FTIR (both polarized and unpolarized) and correcting for differences in calibrations of Paterson (1982) and Bell et al. (2003) as quantified by Koga et al. (2003). A discussion of this is included in Supplementary Material Text S3.

5 Results

5.1 LPO Types

The results of the analytical work conducted on our own samples are provided in Tables 1 and 2. We found that all documented LPO types were represented: 18 samples had A-type, 5 B-type, 3 C-type, 5 D-type, 15 E-type, and 8 AG-type (Figure 2). 11 samples had ambiguous LPOs that could not definitely be categorized into one of these 6 types. Three of these "inconclusive" samples displayed a bimodal C-E-type LPO identical to that explored recently in Wallis et al. (2019).

The 445 peridotite samples from the literature plus our own 65 samples total 510 samples (Figure 2). The frequency of LPO types within this dataset is broadly consistent with the compilation of Ismaïl & Mainprice (1998), which included fabrics for 110 peridotites from a wide range of geologic settings. Our dataset includes a smaller proportion of A-type samples than this prior compilation (29% versus 50%) with more representation of the other LPO types; this is likely a reflection of community interest in these more "exotic" LPO types over the past 15 years. Nevertheless, the observation that our new compilation exhibits the same relative proportions of LPO types as Ismaïl & Mainprice (1998) (where A-type is the most common, followed by D-, AG-, B-, E-, C-types in that order), suggests that these relative abundances may be representative of peridotites globally. There is most likely no sample overlap, as all studies included in our compilation were published after Ismaïl & Mainprice (1998).

5.2 Fabric Strength

The following results refer exclusively to the samples analyzed in this study (and exclude data from the literature compilation). We examined trends relating to fabric strength, or the degree to which grains are aligned, as this is often used as a metric to assess whether an LPO has reached steady state in experiments (cf. Skemer & Hansen, 2016). M- and J-indices range from 0.01–0.37 and 1.2–17.4, respectively. There was a strong agreement between M- and J-indices ($R^2 = 0.72$), with the possible exception of D-type samples, whose M-indices appeared to overpredict relative to the J-index (Supplementary Material Figure S3). There did not appear to be any strong correlation between olivine LPO type and fabric strength.

5.3 Modal Percentages

We examined whether the modal percentage of olivine affects the LPO type, since the presence of other phases (namely clinopyroxene and orthopyroxene) may inhibit the formation of LPO in olivine through a mechanism such as Zener pinning (Smith, 1948). Olivine modal percentages for the peridotites studied range from 45 to 100% (with the exception of one olivine gabbro with 28% olivine). We found no relationship between olivine LPO type and modal percent with the exception of D-type, which seemed to occur over a narrower range of modal percentages (Supplementary Material Figure S3).

5.4 Microstructural Categories

Within our own suite of 65 samples, 16 were classified as protogranular, 31 as porphyroclastic, 15 as mylonitic, and 3 as ultramylonitic (Table 1). We examined whether olivine LPO type is affected by microstructural category, as this may be a proxy for strain magnitude, and strain magnitude has been suggested to influence LPO development within both naturally and experimentally deformed peridotites (e.g. Warren et al., 2008; Hansen et al., 2014). While we see no evidence that LPO varies by microstructural category globally (Supplementary Material Figure S4), there are two individual localities for which olivine LPO does seem to correlate with microstructure category. In the suite of Mojave xenoliths, for example, granular and protogranular samples (i.e., low strain) consistently preserve A-type LPO whereas porphyroclastic and mylonitic samples (i.e., high strain) typically displayed E-type LPO. In the suite of high temperature xenoliths from Lunar Crater volcanic field

(cf. Dygert et al., 2019), highly strained ultramylonitic samples display either C-type LPO (or an unusual bimodal C-E-type hybrid that resulted in some samples being listed as "inconclusive," Supplementary Material Table S5), while the lower strained porphyroclastic samples preserve E-type LPOs.

5.5 Slip Systems

To confirm whether our LPOs reflect deformation along particular slip systems, we performed subgrain misorientation analysis to determine the slip systems active for specific porphyroclasts containing subgrain boundaries (Supplemental Material Text S4 and Figure S6). Evidence for all known olivine slip systems – [100](010), [001](010), [001](100), and [100](001) – was identified within this dataset; [100](010) and [100](001) were the most common. The results of these analyses reveal a complicated relationship between LPO type and active slip systems, with many samples exhibiting subgrain misorientation patterns indicative of incompatible slip systems (Figure 4). With few exceptions, LPOs plotted for subsets of small (recrystallized) and large (porphyroclasts) grains both reflect the same bulk LPO, suggesting that these contradictory slip systems do not simply reflect a new LPO developing in the most recent stage of deformation. Interestingly, only one sample with B-type LPO had subgrains preserving the [001](010) slip system, as would be expected for dislocation creep under simple shear.

5.6 Water Content

Samples in this study record measured water contents for olivine, orthopyroxene, and clinopyroxene of 1–87 ($n = 38$), 11–318 ($n = 27$) and 53–1712 ($n = 24$) ppm H_2O (16–1392, 121–3498, 636–20544 ppm H/Si) respectively, and calculated olivine water contents (from partition coefficients with pyroxenes) of 3–75 ppm H_2O or 48–1200 ppm H/Si ($n = 30$). Plots of olivine versus pyroxene water contents rarely agree with experimental partitioning predictions (Figure 5). This observation supports the notion that measured olivine water content is an unreliable indication of *in situ* mantle water contents in xenoliths (cf. Warren & Hauri, 2014). The strong agreement between orthopyroxene and clinopyroxene water contents, and its consistency with experimental partition coefficients, supports the assumption that pyroxenes do preserve *in situ* water. Additionally, we saw no systematic variation between core and rim measurements in pyroxenes (Figure 5) and water content transects

showed no systematic diffusion of water in these phases. Only core measurements were used to calculate the average water contents for each phase presented in Table 1.

5.7 Deviatoric Stress, Temperature, and Strain Geometry

Stresses estimated using paleopiezometry range from 11–87 MPa and deformation temperatures range from ∼600–1258°C. The wide range of values calculated for olivine thin section-derived Flinn constant, k, as well as the spinel CT-derived shape parameter, T, suggest these samples represent a wide range of strain geometries: k and T ranged from 0.04–5.8 ($n = 24$) and −0.87–0.77 ($n = 42$), respectively (P' ranged from 1.16–2.85) (Figure 8 and Table 2).

6 Comparisons Between LPOs and Deformation Parameters

6.1 Water vs. Stress

Figure 6 demonstrates that LPO types do not neatly segregate into LPO clusters in water-stress space, as suggested based on the experiments represented in Figure 1. For example, all LPOs are present in the region where only A-type is predicted (low water and low stress). Furthermore, although the highest water content samples are C-type, they still fall well below the experimental E-to-C transition. The observations disagree with the experimental relationships shown in Figures 1 and 6. Some trends do, however, emerge. Two that agree with experimental predictions are (1) natural samples with the highest water contents have C-type LPOs, and (2) A-type LPO does not occur at water contents above the experimental A-to-E-type boundary.

6.2 Stress vs. Temperature

Experiments indicate that the transition from B- to C-type LPO can be dependent on temperature and stress, with B-type occurring at lower temperatures and higher stresses (Katayama & Karato, 2006). Figure 7 reveals that C-type LPO does seem to be associated with higher temperatures and rarely occurs in peridotites with temperatures below 800°C. The B-type samples, however, occur over a very wide range of both stress and temperature. High pressure conditions (as inferred from the presence of garnet) appears to have no effect on the relationship between B and C-type LPO in stress-temperature space, and can therefore likely be ruled out as the sole reason for high temperature B-type samples. When

averaged over all samples, B and AG-type samples have the lowest average temperatures (∼850°C), while E-type has the highest (∼1000°C). The average temperatures recorded in samples with A, C, and D-type LPOs are all similarly ∼900–950°C.

6.3 Effect of Strain Geometry

The Flinn constant, k (see Section 3.3), derived from olivine SPO measurements revealed no trend with the type of olivine LPO — that is, whether some olivine LPOs preferentially form in prolate (constriction) vs. oblate (flattening) strain geometries. Interestingly, k also showed very little agreement with the shape parameter, T, derived from spinel grains (Supplementary Material Figure S3). This lack of agreement, along with the observation that we *do* see a trend between LPO and spinel shape, may mean that in many samples, olivine SPO does not reliably preserve strain geometry, possibly due to dynamic recrystallization.

The trend between LPO and spinel-recorded strain geometry is illustrated in Figure 8. Chatzaras et al. (2016) observed an inverse trend between BA-index and spinel shape parameter, T, consistent with AG-type ($0 < \text{BA} \lesssim 0.35$) forming under flattening (oblate ellipsoid: $T > 0$), orthorhombic LPO types ($0.35 \lesssim \text{BA} \lesssim 0.65$) forming under plane strain ($T \approx 0$), and D-type ($0.65 \lesssim \text{BA} < 1$) forming under tension or constriction (prolate ellipsoid: $T < 0$). When plotted together with the samples in this study, we find that this relationship persists in most cases, with the exception of B- and C-type LPOs, which consistently fall in the oblate category (Figure 8b).

7 Discussion

7.1 Uncertainties

Before we compare and contrast the natural and experimental datasets, we first evaluate the various sources of uncertainty that may influence our natural data, including three primary sources: 1) analytical, 2) calibration and standards-related, and 3) epistemic uncertainties (i.e., uncertainties related to lack of knowledge) regarding whether the measurements are representative of deformation conditions.

7.1.1 Analytical Uncertainties

Analytical uncertainties within our own dataset are minimal. In pyroxenes, the standard error for each measurement was only 1% of the measured water content. The uncertainty from water content measurements is primarily due to heterogeneity of grains within each sample, which resulted in a standard error of ∼15% of the reported average water contents in pyroxenes. Within our own dataset, the SIMS calibration curves generated from established water content standards have relatively low levels of uncertainty. The standard error of the regression line fit through the four calibration curves ranged from 18–22 ppm H_2O ($R^2 = 0.96 - 0.98$) with the exception of one mount where the standard error was 41 ppm H_2O ($R^2 = 0.89$) (Supplementary Material Figure S1). The uncertainties around stress estimates from paleopiezometry can similarly be estimated from the variations in recrystallized grain sizes within each sample; they amounted to an average standard error of < 2 MPa. Analytical standard error of temperature measurements are similarly low. While no new temperature estimates are presented in this study, temperatures from the Mojave xenoliths, for example, have a standard error of 2–12°C (Bernard & Behr, 2017). We therefore do not consider the analytical uncertainties to be large enough to explain any discrepancies between nature and experiments.

7.1.2 Uncertainties in Calibrations

In the case of water contents measured in olivine and/or pyroxenes with FTIR, different calibrations yield significantly different water content estimates. The calibration of Paterson (1982) used in many natural studies as well as in the LPO experiments represented in Figures 1 and 6 does not take into account mineral orientation, and therefore underpredicts olivine water contents by a factor of ∼3.5 and orthopyroxene water contents by a factor of ∼2 compared to the more accurate and precise calibration of Bell et al. (2003), which is consistent with SIMS measurements (Koga et al., 2003). These calibration issues affect all of the experimental data, and many of the natural datasets which we incorporated from previously published work. They do not, however, affect our own data measured using SIMS, so correlations or decorrelations related to water in our own dataset are robust. When plotting data from the literature, we have attempted to overcome this issue by multiplying any FTIR water contents calculated with the Paterson (1982) calibration so that they are in line with the calibration of Bell et al. (2003), using the aforementioned correction factors. In addition to these calibration issues, there are also different estimates of the partitioning

coefficients between olivine and pyroxenes (e.g. Hirth & Kohlstedt, 1996; Warren & Hauri, 2014). All of the data we discuss were corrected using the same partitioning coefficient, however, so these are systematic uncertainties that affect all data points equally.

7.1.3 Epistemic Uncertainties

There remains a recurring difficulty in natural microstructural datasets of relating geochemistry to deformation stages. Peridotite mineral geochemistry, including hydrogen used to measure water content and major and trace elements used for thermometry, can be reset during both the short timescales of xenolith ascent, but also during longer timescale thermal events that can occur while the rocks are still *in-situ* in the mantle, but not necessarily deforming. Longer timescale thermal events can induce hydrogen diffusion even in pyroxenes. Simultaneously, however, prolonged periods of heating should also affect the microstructural evolution, and and we should expect pre-existing deformation fabrics to show signs of annealing/grain growth if they were being heated *in-situ*, but not simultaneously deforming. Comparisons of H diffusion rates in pyroxene to olivine grain growth rates, suggest that both should be significant over ky timescales (Supplementary Material Text S8 and Figure S9). For example, experiments of Ingrin et al. (1995) suggest that at 900°C, water in diopside can diffuse ∼1 meter in 20 ky; and the wet grain growth law of Karato (1989) predicts several mm of grain growth for those same conditions and timescale. Samples with granular textures and relict LPOs are likely examples of this scenario, but the other textures in our dataset retain grain morphologies that argue against significant thermal annealing, thus suggesting the measured water contents are representative of water content during deformation. Only half of the studies included in the compiled external datasets, however, interpreted temperature as representative of deformation temperatures specifically (Supplementary Material Text S7).

7.2 Explanations for Differences Between Nature and Experiment

As discussed in Section 6, our natural dataset does not exhibit systematic relationships between most olivine LPO types and deformation conditions such as stress magnitude, water content or temperature. Here we explore three potential explanations for this, including the following:

413 *1. At the low stresses of the natural samples examined, olivine slip systems are not*
414 *strongly sensitive to external deformation conditions.*

415 Differential stresses in the experiments connecting olivine LPO to water, temperature,
416 and stress magnitudes range from ∼100 to 500 MPa (Bystricky et al., 2000; Zhang et al.,
417 2000; Jung & Karato, 2001; Katayama et al., 2004; Jung et al., 2006). In contrast, how-
418 ever, the vast majority of natural samples examined here record stresses < 100 MPa and
419 cluster around 30 MPa (Figures 6 and 7). Several experiments have been conducted at
420 similarly low differential stresses (∼10–180 MPa) on olivine single crystals at relatively high
421 temperatures (∼1200–1600°C) and room pressures (Durham & Goetze, 1977; Bai et al.,
422 1991; Jin et al., 1994). These experiments did not detect any difference in the stress expo-
423 nents for the [100](010), [100](001), and [001](100) olivine slip systems, suggesting a lack of
424 stress dependence on slip system activity at these conditions. The similar lack of system-
425 atic correlation between LPO type, and water or temperature in our natural dataset also
426 suggests that these components of deformation conditions only weakly influence olivine slip
427 systems at low stresses. An exception may be the [001](100) slip system characteristic of
428 C-type LPO, as this LPO type appears to correlate with the experimentally constrained
429 boundary in stress-temperature space. Mackwell et al. (1985) conducted T = 1300°C,
430 P = 0.3 GPa deformation experiments on San Carlos olivine single crystals and found that
431 water had no effect on the dominant slip system. However, it should be noted that water-
432 induced fabric transitions may not occur readily at these low pressures since water solubility
433 in olivine increases with pressure (Kohlstedt et al., 1996). At low stresses, alternative fac-
434 tors may instead influence relative strength of slip systems. For example, the relatively low
435 stress single crystal deformation experiments of Raterron et al. (2009) suggest that high
436 pressure – rather than water, stress, or temperature – may promote to a transition from
437 A-type [100](010) to B-type [001](010) slip.

438 *2. Apparent LPO type is more a reflection of kinematics and strain path than differ-*
439 *ences in slip system strength.*

440 A weak sensitivity of olivine slip systems to deformation conditions at low stresses is
441 compatible with (and perhaps required by) the results shown in Figure 8a in which olivine
442 LPO exhibits a significant correlation with spinel shape. That is, if olivine slip systems are
443 only weakly influenced by external deformation parameters, then olivine LPO should become
444 much more sensitive to boundary conditions and strain path (also referred to as “strain

geometry"). A sensitivity of LPO to strain geometry has been recognized in numerous experimental and modeling studies of a wide range of crustal minerals including quartz, calcite, biotite, and hornblende (e.g. Lister & Hobbs, 1980; Lloyd et al., 2011; Llana-Fúnez & Rutter, 2014). The relationship between LPO and strain geometry has also been explored for olivine, primarily through modeling and investigations of natural peridotites. For example, numerical simulations by both Wenk et al. (1991) and Tommasi et al. (1999) found AG-type LPO formed in axial compression or flattening strain, while A-type LPO formed in simple shear, and D-type formed in transtension or constrictional strain. Chatzaras et al. (2016) found the same relationship between these LPOs and strain geometry in a suite of natural samples from West Antarctica, and additionally found evidence that B-type LPO forms in flattening strain, an observation also made in natural samples by Lee & Jung (2015).

The role of strain geometry has been addressed less commonly in experiments, although multiple studies have produced AG-type LPO during axial compression experiments (e.g. Nicolas et al., 1973; Hansen et al., 2011). The vast majority of olivine deformation experiments, including those associating olivine LPO types to deformation conditions (Figure 1), are conducted under simple shear. The five slip systems producing A- through E-type LPOs in simple shear produce very different LPO patterns under triaxial compression and extension (Fig. 4 in Skemer & Hansen (2016)).

A sensitivity to strain geometry also means that the orientation of pre-existing LPOs in the mantle will play a significant role in determining both the evolution of LPO and the final LPO at steady state. Deformation experiments have historically been conducted on randomly oriented hot-pressed aggregates with weak to no pre-existing LPO. However, modeling (e.g. Becker et al., 2006; Skemer et al., 2012; Boneh et al., 2015), experiments (e.g. Skemer et al., 2011; Boneh & Skemer, 2014; Hansen et al., 2014, 2016), and natural studies of exposed peridotite shear zones (e.g. Warren et al., 2008; Skemer et al., 2010; Webber et al., 2010; Hansen & Warren, 2015) have shown that pre-existing LPO and changes in kinematics influence subsequent LPO development. Boneh et al. (2015), for example, showed that models with pre-existing textures evolved differently with progressive strain in each of three kinematic configurations, and differently from scenarios with initially random textures. This modeling is consistent with experiments by Boneh & Skemer (2014), where Åheim dunite, a starting material with moderately strong texture, was deformed and compressed in three directions (parallel, perpendicular, and oblique) relative to its initial foliation. When the starting texture is random, samples compressed perpendicular to foliation developed the

expected AG-type LPO in both the models of Boneh et al. (2015) and the experiments of Boneh & Skemer (2014). Interestingly, when there was a pre-existing texture – particularly in the oblique and parallel configurations – an unexpected LPO formed where [100] axes preferentially oriented perpendicular to lineation within the foliation plane. While B-type in appearance, this LPO was a transient consequence of the reorientation of a pre-existing fabric, and not a product of the [001](010) slip system. In this case, the "B-type" LPO would have no relationship to the high stress, moderate-high water contents or low temperatures predicted by simple shear experiments. Rather, it was a consequence of kinematic factors.

None of the configurations in the Boneh & Skemer (2014) experiments, which were only conducted to strains of < 0.7, reached a steady state, making it unclear how long this transient pseudo LPO type would persist with increased strain. Experiments by Hansen et al. (2014, 2016) that deformed samples to much higher strains ($\gamma = 20$) demonstrated that the orientation and strength of LPOs are identical regardless of any pre-existing texture (formed through tension followed by torsion) when $\gamma \gtrsim 10$. Steady state did, however, appear to require higher amounts of strain in samples with pre-existing textures, in agreement with the findings of the aforementioned numerical and natural studies. Models with pre-existing textures can require 3–5 times the strain magnitude to approach steady state, and experimental and field data suggest a shear strain of 1 is required to align [100] parallel to shear directions in samples without pre-existing LPO and as much as 4 for samples with initial textures (Skemer & Hansen, 2016, for a review).

Since the majority of our samples are xenoliths, it is impossible to know if steady state LPO has been achieved, or to quantify the strain magnitude in each sample. It is likely that many of these lithospheric peridotites have not achieved steady state, as moderately strained ($\gamma = 2$–4) portions of exposed mantle shear zones have not reached steady state as evident by the oblique orientation of [100] axes to shear (Skemer & Hansen, 2016).

3. At the low stress magnitudes of the natural samples examined, olivine LPOs are not primarily controlled by slip on individual slip systems but instead by activation of other deformation mechanisms that operate to allow strain compatibility.

This explanation is compatible with our observations presented in Figure 4, in which inferred active slip systems in some samples do not match the expected slip system for the observed bulk LPO type in the same sample. The mismatch is especially prominent for B- and AG-type samples, whereas A-, D- and E-type display misorientation profiles consistent

with their expected [100] slip systems. (The sparse number of C-type samples, particularly those with subgrains, makes it difficult to draw conclusions about its connection with the associated [001](100) slip system.)

As described previously, both B- and AG-type LPO types have been associated with factors other than activation of the assumed [001](010) and $[h0l](010)$ slip systems, respectively. AG-type has been associated with deformation in the presence of melt (Holtzman et al., 2003; Qi et al., 2018), and – in addition to forming transiently (Boneh & Skemer, 2014; Boneh et al., 2015) or from flattening strain (Chatzaras et al., 2016) – B-type LPO has been attributed to a deformation through grain size sensitive deformation mechanisms such as diffusion creep (Sundberg & Cooper, 2008; Drury et al., 2011; Miyazaki et al., 2013) and dislocation-accommodated grain boundary sliding (DisGBS) (Précigout & Hirth, 2014).

Of course some of the noise present in Figure 4 may be attributed to combinations of slip systems working in concert to produce LPOs, in agreement with modeling that incorporates combinations of critical resolved shear stresses for the [100](010), [100](001), [001](010), and [001](100) slip systems (e.g. Kaminski, 2002; Becker et al., 2008). In particular, it may be unsurprising that so many samples preserve subgrains with both [100](010) and [100](001) slip systems, as these have nearly identical critical resolved shear stresses at intermediate temperatures ∼1000°C (Goetze, 1978). Alternatively, because misorientation profiles are necessarily collected from porphyroclasts, perhaps they reflect the orientations of harder crystal slip systems whereas the recrystallised grains (lacking subgrains) are those that experienced slip along the system representative of the bulk LPO.

The three explanations discussed above are not mutually exclusive. Moreover, our data and the explanations provided above do not imply that deformation conditions (such as stress, temperature, and water) have no effect on olivine slip systems, but rather that boundary conditions and pre-existing fabrics appear to be more influential than deformation conditions on olivine LPO in the ambient lithospheric mantle. These findings suggest caution should be taken in using olivine LPO types to infer deformation conditions without independent deformation condition constraints.

7.3 Implications for Seismic Anisotropy

As suggested by the smaller proportion of A-type samples in our dataset versus the compilation of Ismaïl & Mainprice (1998) in Figure 2, there may be a bias in favor of non-

A-type LPOs in the literature due to the community's interest in these less common types in recent decades. This issue of representation aside, we use this large dataset to investigate the implications for seismic anisotropy, particularly in the continental lithospheric mantle, as this is where the vast majority of samples are sourced (Figure 2). One of the most striking aspects of this dataset is the number of different olivine LPOs preserved at individual localities (Figure 3). 19 of the 52 localities had samples with three or more LPOs, 18 had B-type LPOs, and 14 had LPO types with opposing/orthogonal fast axes: that is, B-type LPO in addition to A, C, D, and/or E-type LPOs. Lastly, while over a quarter of localities (15) had samples with C-type LPOs, less than half of those had more than two individual samples with this LPO type. These observations have four primary implications:

1. The relatively complex seismic anisotropy patterns observed in the continental (versus oceanic) mantle (e.g. Long & Becker, 2010) can be explained in part by the wide range of LPO types found among the peridotites sampled from xenoliths and continental massifs. Some of this complexity may be due to frozen-in anisotropy within the lithosphere, but our reseults suggest it could also be attributed to the lack of stress dependence of slip systems at low stresses typical of the upper mantle, small scale variations in strain geometry, the influence of pre-existing textures on LPO development, or all of the above. While trends of LPO type with estimated depth goes beyond the scope of this study, it is conceivable that the wide variety of LPO types at some individual localities may vary with depth, which would be in agreement with recent studies that observe complex anisotropic layering within the lithosphere (e.g. Ford et al., 2016) and connect mid-lithospheric discontinuities (MLDs) to sharp changes in seismic anisotropy (e.g. Yuan & Romanowicz, 2010; Wirth & Long, 2014; Auer et al., 2015).
2. The complexities introduced by B-type LPOs affect more tectonic settings than just the cold corner of the mantle wedge. This may be an explanation (though one of several, see Long (2013) for a review) for the confounding occurrence of trench parallel anisotropy unexpectedly far away from the trench (e.g. Hoernle et al., 2008; Abt et al., 2009, 2010; Long et al., 2015). In our dataset, B-type LPO is shown to develop at the full range of mantle stress, water, and temperature conditions (up to 1100°C). For this reason, flow-perpendicular fast directions may be more common than previously assumed.

3. The common co-occurrence of LPO types with orthogonal fast directions that would cancel each other out might mean that at many places, we could expect to see no net azimuthal anisotropy. Additionally, while AG-type — a common LPO type in this dataset — results in a strong alignment of olivine's slow axis ([010]) aligned normal to flow, we would expect no azimuthal anisotropy as both its fast and intermediate axes ([100] and [001]) are girdled (and therefore unoriented) within the foliation or flow plane. Together, this would suggest that a lack of azimuthal anisotropy in a particular region should not be interpreted as a lack of deformation through dislocation creep, particularly if radial anisotropy is also observed.
4. In the upper mantle, on average, horizontally polarized seismic shear waves (SH) travel faster than vertically polarized ones (SV). C-type LPO is the only variety that is predicted to substantially affect this radial anisotropy, since its alignment of fast axes orthogonal to the flow plane would result in $V_{SV}>V_{SH}$ rather than $V_{SH}>V_{SV}$ (in the case of horizontal shear), which is characteristic of all other LPO types. However, C-type LPO is not only the least abundant LPO type in the dataset, but when observed, it was typically only present in one or two samples at a given locality. This suggests that despite the complexities in azimuthal anisotropy resulting from the confluence of these various LPO types at localities around the globe, radial anisotropy may be largely unaffected. An exception might be the large subset of samples with E-type LPO, as this type results in a $\sim$30% reduction of radial anisotropy compared to A-type LPO (Becker et al., 2008).

8 Conclusions

We present a compilation of new and published naturally deformed peridotites with the goal of connecting six established olivine LPO types to the wide range of deformation conditions present in the Earth's mantle. Contrary to previous inferences from experiments, we do not see evidence that olivine LPO is primarily determined by water content and differential stress magnitude, possibly because individual olivine slip systems are less sensitive to stress and water content at the low stress magnitudes that characterize the upper mantle. Temperature appears to play a role, with AG- and B-type LPOs occurring at lower temperatures on average, and C- and E-type LPOs dominantly occurring at higher temperatures. Additionally, quantification of strain geometry reveals that AG-, B- and C-type LPOs typically form when deformation fabrics are oblate, D-type when prolate, and A- and E-type

during plane strain. Our results highlight the need for further experiments investigating the relationship between LPO, stress, and water, but at conditions closer to those typical of the upper mantle (i.e., lower stress and temperatures) and with improved constraints on water contents using the calibration of Bell et al. (2003) or SIMS. Finally, our results showcase the complexities of olivine LPO development. The observation that individual localities can preserve as many as five LPO types exemplifies this, and may explain some of the complexities observed from seismic anisotropy within the continental mantle lithosphere.

Appendix A: List of Studies Included in the Literature Compilation

Samples from the following studies are represented in the literature review: Bascou et al. (2008); Baptiste et al. (2015); Behr & Smith (2016); Cao et al. (2017); Chatzaras et al. (2016); Chin et al. (2016); Drury et al. (2011); Falus et al. (2008); Frese et al. (2003); Hidas et al. (2007); Jung et al. (2009a,b, 2013, 2014); Kaczmarek & Reddy (2013); Kamei et al. (2010); Katayama et al. (2005, 2011); Kim & Jung (2015); Lee & Jung (2015); Mehl et al. (2003); Michibayashi et al. (2007, 2012); Michibayashi & Oohara (2013); Mizukami et al. (2004); Mizukami & Wallis (2005); Morales & Tommasi (2011); Nagaya et al. (2014); Palasse et al. (2012); Park & Jung (2015); Park et al. (2014); Pera et al. (2003); Précigout & Hirth (2014); Satsukawa et al. (2010); Satsukawa & Michibayashi (2014); Skemer et al. (2010, 2013, 2006); Soustelle et al. (2010); Tasaka et al. (2008); Tommasi et al. (2006, 2004); Vauchez et al. (2005); Wang et al. (2013a,b); Warren et al. (2008); Webber et al. (2010); Xu et al. (2006); Yang et al. (2010).

A description of how information was incorportated from these studies, along with an inventory of the types of samples and analyses done in each of these studies can be found in the Supplementary Material (Text S3 and Table S4).

Acknowledgments

This research was supported by a National Science Foundation (NSF) Graduate Research Fellowship made to R.E. Bernard and a NSF grant (EAR-1251621) awarded to W.M. Behr. We are grateful to the UTCT facility at UT Austin for assistance with X-ray CT, Rick Hervig for assistance with SIMS, and Jed Mosenfelder for loaning SIMS standards. We also thank the UT Austin Jackson School of Geosciences and the Smithsonian National Museum

635 of Natural History, which both loaned us several samples. Data presented in this manuscript
636 can be accessed through the Texas ScholarWorks repository (doi:10.15781/T2VQ2SW1G).

Figure 1. Five types of olivine LPO are shown with pole figures and schematic oriented crystals in water vs. stress space as determined from the experiments of Bystricky et al. (2000); Zhang et al. (2000); Jung & Karato (2001); Katayama et al. (2004); Jung et al. (2006). Water contents were calculated using the calibration of Paterson (1982), and would be ~3.5X higher using the calibration of Bell et al. (2003), as is presented in the gray region of Figure 6.

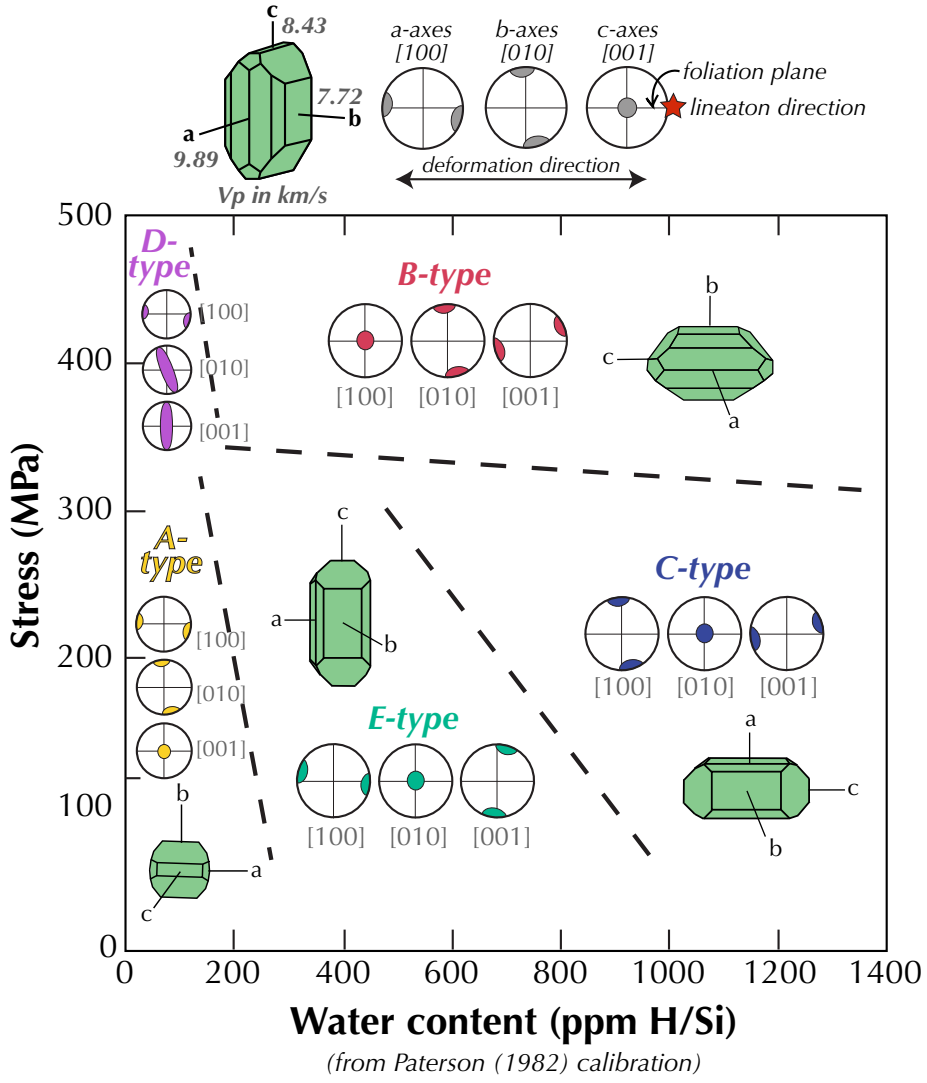

Figure 2. A: Localities of samples analyzed in this study as well as represented in the literature compilation (48 published studies representing 445 peridotite samples from 52 localities). Due to space constraints, a list of these studies and citations can be found in the Supplementary Material. B: A breakdown of the 510 individual samples included in this study and in the literature compilation by peridotite type. C: A breakdown of the 510 individual samples included in this study and in the literature compilation by olivine LPO type. Inset: Pie charts show that a comparison of the proportion of LPO types in this compilation are similar to the compilation of Ismaïl & Mainprice (1998), shown in gray.

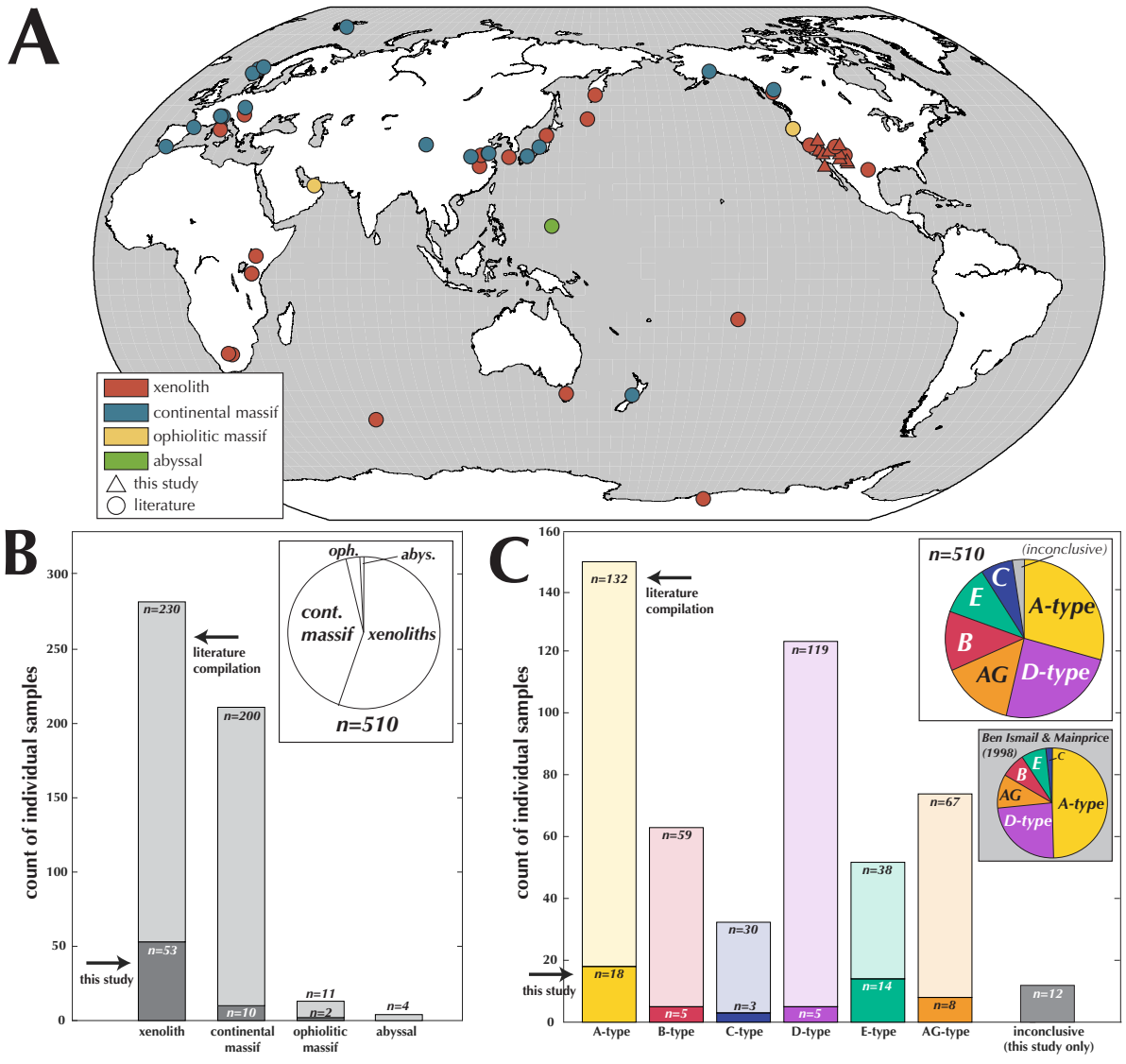

650 **Figure 3.** Frequency of olivine LPO types present at each individual locality. Locality numbers
651 are identified in Table 1 and the Supplementary Material Table S4.

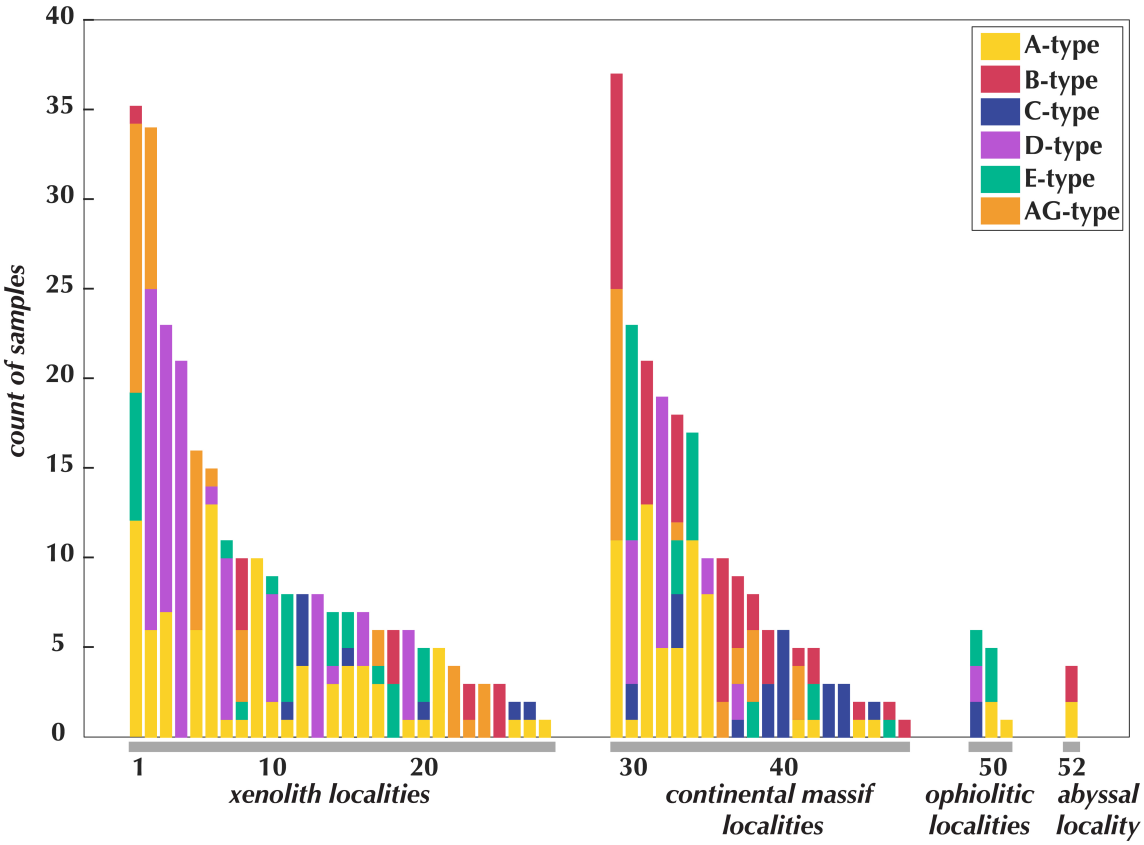

652 **Figure 4.** Bar chart showing the slip systems identified from subgrain misorientation analyses
653 in each sample, which are themselves grouped by the samples' bulk LPO type. Slip systems are
654 colored to match the LPO type associated with each slip system.

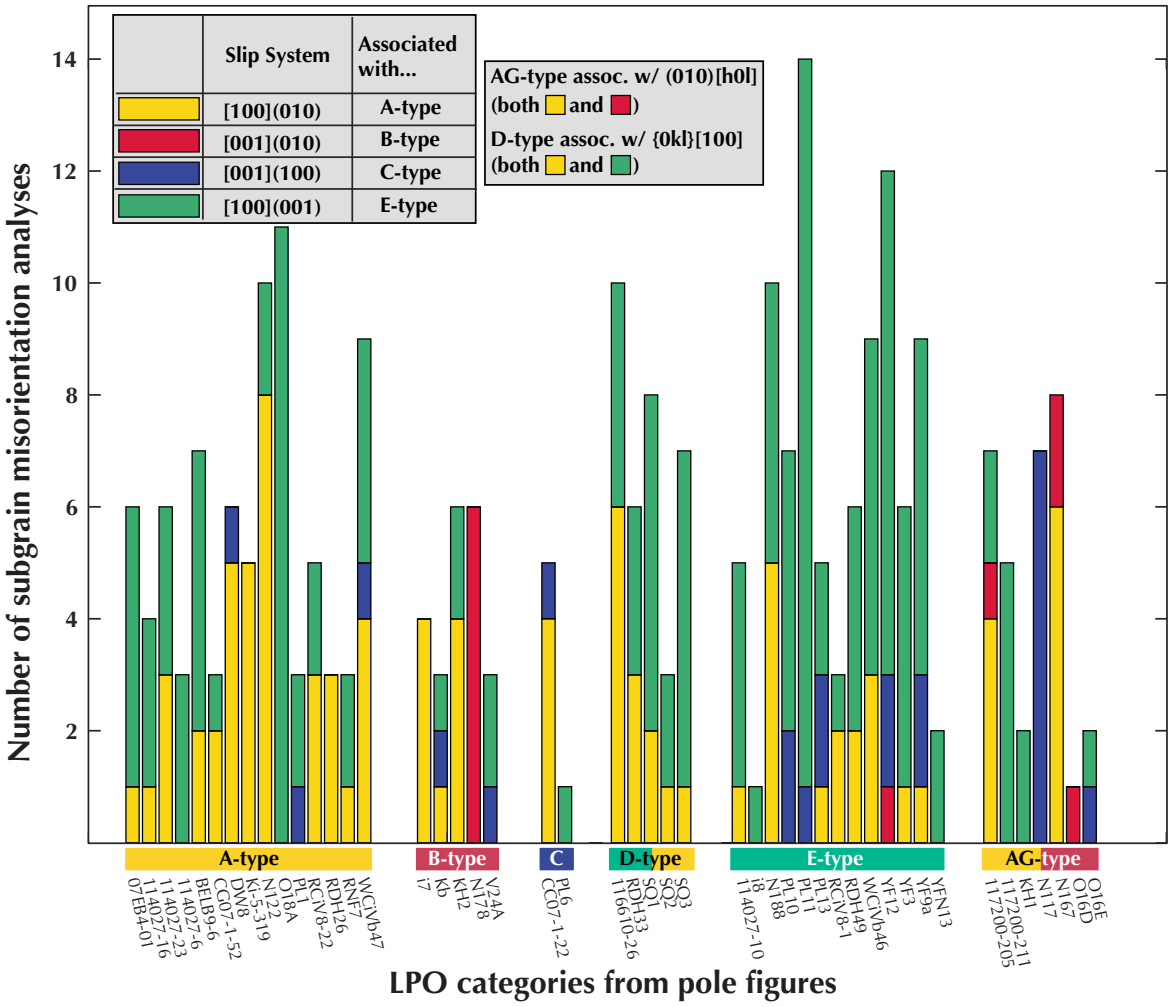

Figure 5. Water contents from this study obtained through SIMS analyses. A-C: Water contents for the three phases are plotted against one another. The samples from this study are plotted alongside the extensive compilation of Warren & Hauri (2014), and the partition coefficients lines of that study based on experimental and natural samples. D: Average core and rim water content values measured for the samples in this study, colored by phase. Inset shows zoomed in view of lower water content values (gray rectangle).

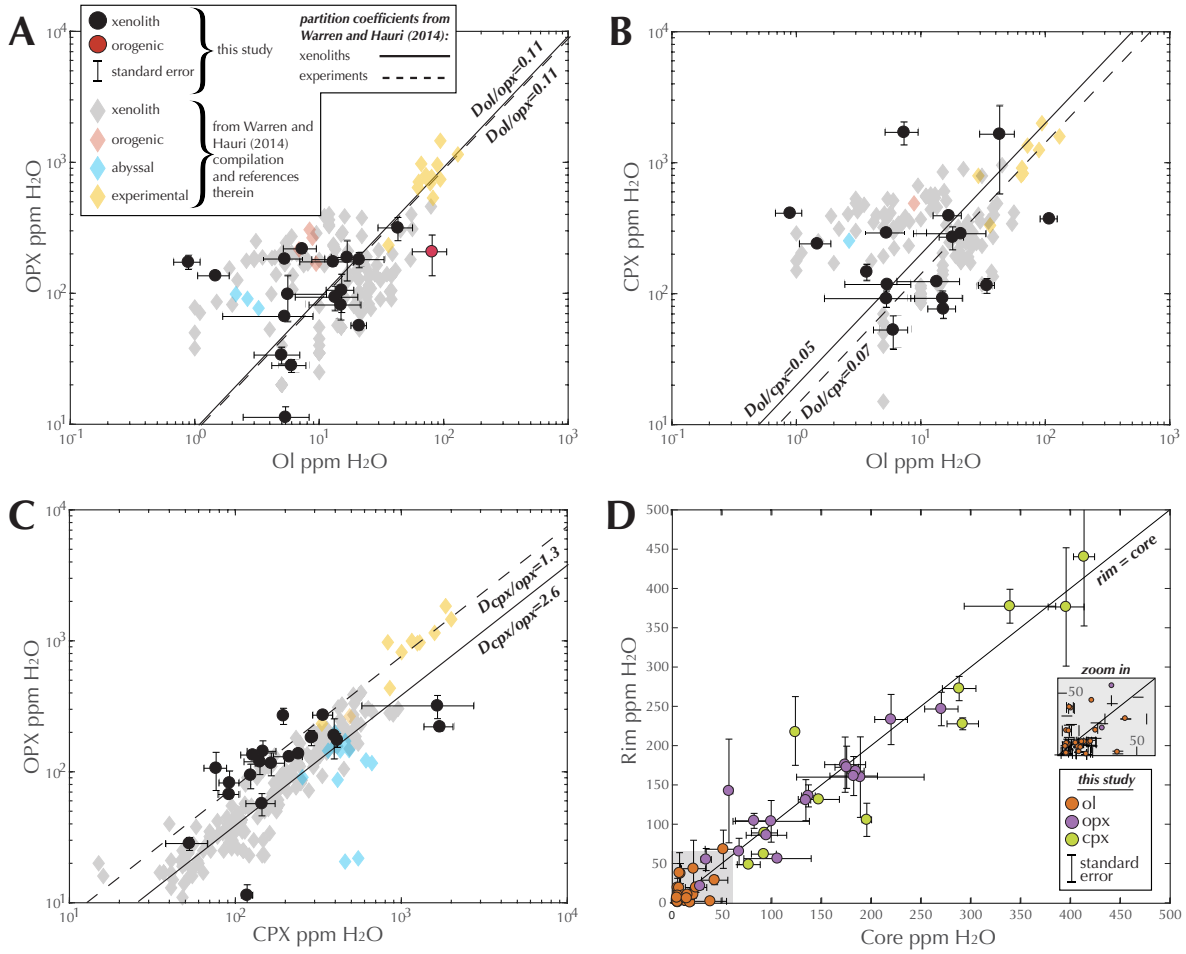

Figure 6. Left: Samples from nature shown along samples from experiments in stress-water space, colored by olivine LPO type. Boundaries projected from experimental conditions to the lower stresses < 100 MPa typical of much of the mantle. All water contents (including that of experiments) that use the Paterson (1982) calibration have been multiplied by 3.5. Most olivine water contents plotted here are calculated from pyroxene water contents using partition coefficients (see text for details). Right: Mean, median, upper and lower quartiles of stress and water for natural samples in each LPO group. (Versions of this figure that are solely on measured vs. calculated water are included in Supplementary Material Figure S5.)

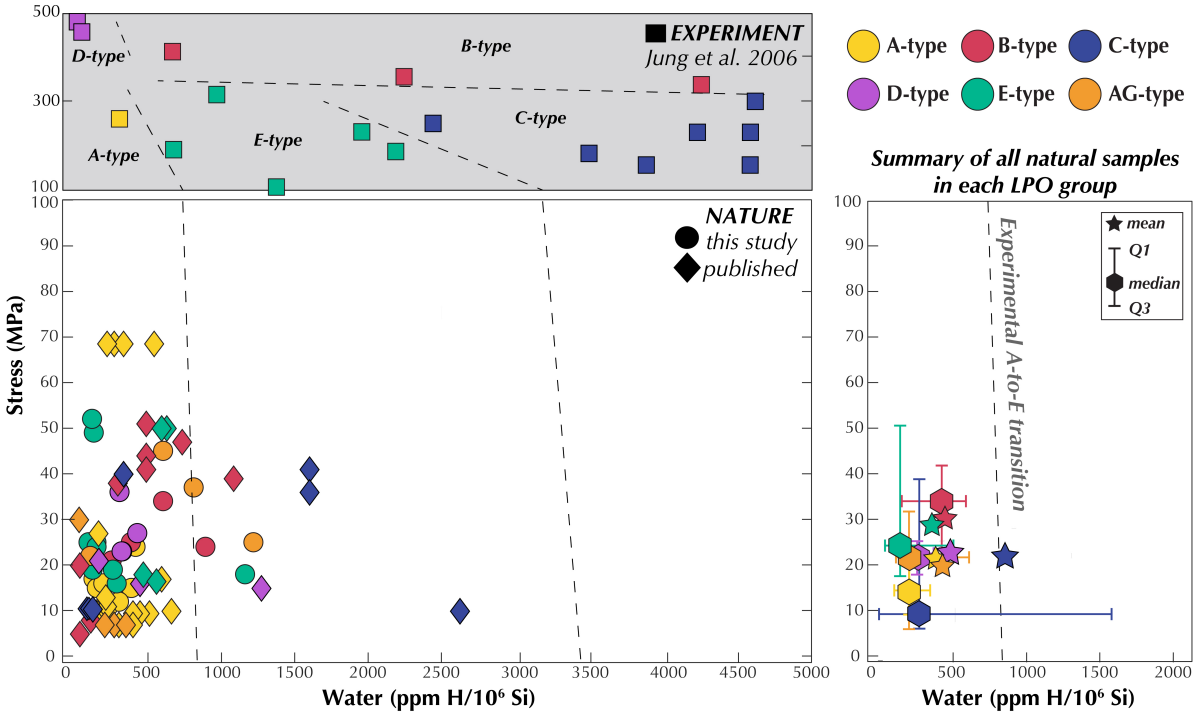

Figure 7. A: Samples in stress-temperature space, colored by olivine LPO type. B: B- and C-type LPO samples from nature shown along samples from experiments. C: Mean and median of stress and temperature for samples within each LPO type group. Lines represent upper and lower quartiles.

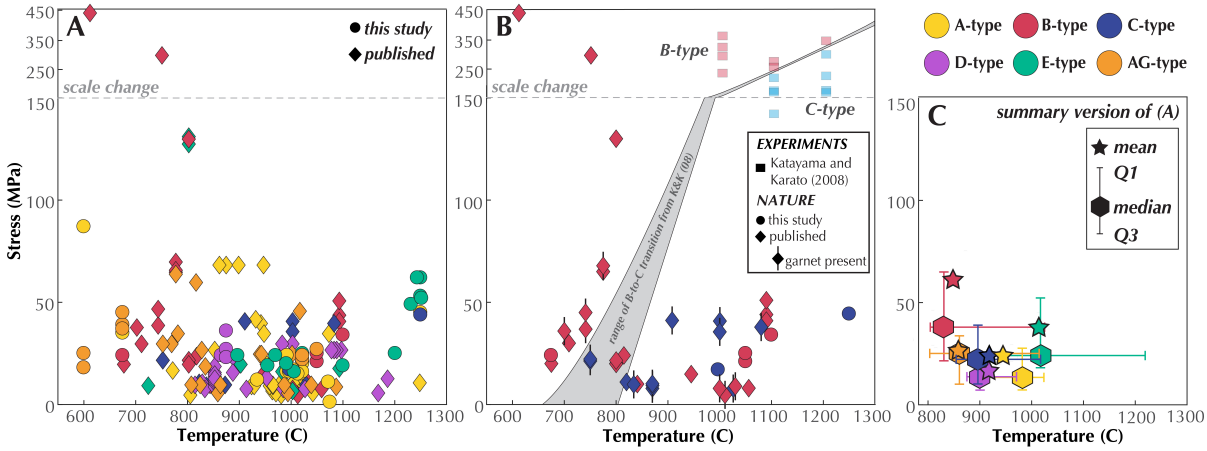

Figure 8. A: Olivine LPO type as a function of spinel shape parameter, T, and BA-index. T increases from prolate to oblate, where 0 is plane strain. Red dashed lines highlight inverse trend originally identified in Chatzaras et al. (2016). B: The same plot, but for mean and median of samples within each LPO type group. Lines represent upper and lower quartiles.

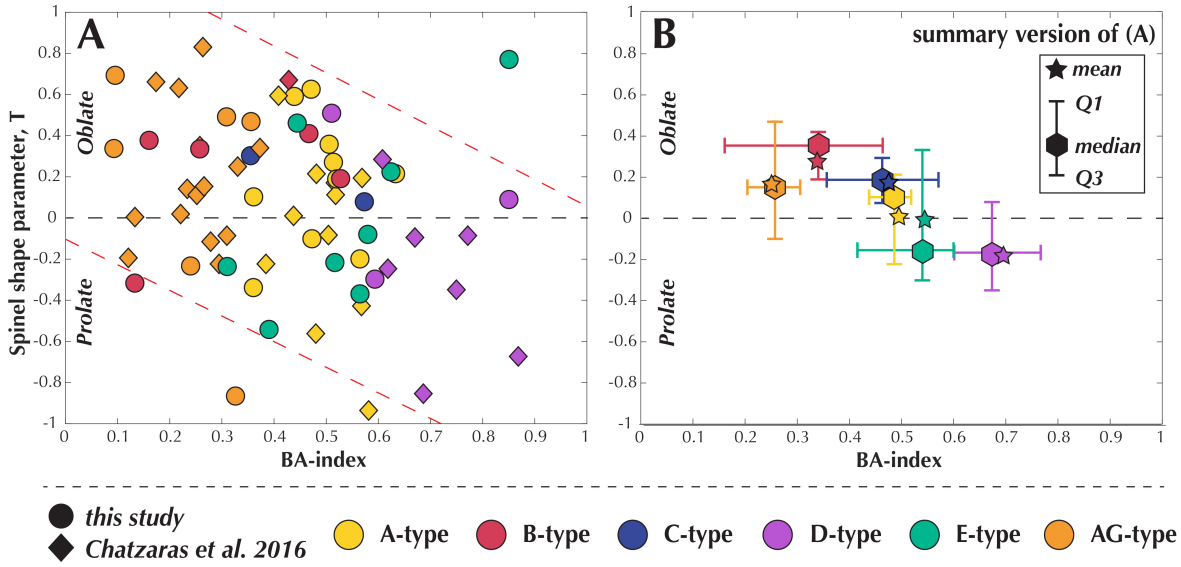

677

Table 1. Properties of analysed samples

							Temperature ‡		Water Content				
Sample No.	**Locality Name**	**Locality No.**	**Peridotite type***	**LPO-type ✣**	**Microstructural category**	**σ (MPa) †**	**T °C (used in plots)**	**T °C range**	**Method ▼**	**OL ppm H_2O (measured) ▲**	**OL ppm H_2O (calculated) △**	**OPX ppm H_2O**	**CPX ppm H_2O**
07EB4-1	Elephant Butte	12	X	A	protogranular	15	1018	---	SIMS	17	24	189	395
114027-10	San Carlos	17	X	E	protogranular	25	1022	988–1056	SIMS	13	10	94	124
114027-16	San Carlos	17	X	A	porphyroclastic	21	1022	988–1056	---	---	---	---	---
114027-23	San Carlos	17	X	A	porphyroclastic	20	1022	988–1056	SIMS	5	5	11	118
114027-6	San Carlos	17	X	A	protogranular	16	1022	988–1056	SIMS	6	11	99	---
116610-26	San Quintin	7	X	D	porphyroclastic	23	875	800–950	SIMS	5	20	184	292
117200-205	San Carlos	17	X	AG	porphyroclastic	22	1022	988–1056	SIMS	5	7	67	92
117200-211	San Carlos	17	X	AG	porphyroclastic	24	1022	988–1056	---	---	---	---	---
BELB9-6a	Elephant Butte	12	X	A	porphyroclastic	---	---	---	---	---	---	---	---
CC07-1-22	Cerro Chato	26	X	C	porphyroclastic	17	997	---	SIMS	7	---	---	---
CC07-2-1	Cerro Chato	26	X	?	porphyroclastic	---	997	---	SIMS	6	3	28	53
CG07-1-26	Cerro de Guadalupe	26	X	?	protogranular	---	---	---	---	---	---	---	---
CG07-1-36	Cerro de Guadalupe	26	X	?	porphyroclastic	---	---	---	---	---	---	---	---
CG07-1-52	Cerro de Guadalupe	26	X	A	porphyroclastic	---	---	---	---	---	---	---	---
DW8	Eifel Germany	28	X	A	protogranular	12	935	900–970	SIMS	18	19	---	271
I7	Ivrea Zone	47	C	B	porphyroclastic	34	1100	1000–1200	SIMS	38	---	---	---
I8	Ivrea Zone	47	C	E	protogranular	19	1100	1000–1200	SIMS	8	---	---	---
Kb	Kilbourne Hole	23	X	B	porphyroclastic	21	1050	1000–1100	SIMS	1	16	137	241
KH1	Kilbourne Hole	23	X	AG	porphyroclastic	27	1050	1000–1100	---	---	---	---	---
KH2	Kilbourne Hole	23	X	B	protogranular	25	1050	1000–1100	SIMS	1	24	174	413
Ki-5-319	Cima	15	X	A	mylonitic	---	---	---	---	---	---	---	---
N117	Navajo	8	X	AG	porphyroclastic	18	600	500–700	---	---	---	---	---
N122	Navajo	8	X	A	porphyroclastic	87	600	500–700	---	---	---	---	---
N167	Navajo	8	X	AG	mylonitic	25	600	500–700	SIMS	43	75	318	1657
N178	Navajo	8	X	B	porphyroclastic	---	---	---	---	---	---	---	---
N188	Navajo	8	X	E	protogranular	18	600	500–700	SIMS	7	72	220	1712
O16D	Norway	8	C	AG	protogranular	39	725	700–750	---	---	---	---	---
O16E	Norway	8	C	AG	porphyroclastic	45	725	700–750	SIMS	38	---	---	---
O18A	Norway	8	C	A	porphyroclastic	35	725	700–750	---	---	---	---	---
O18B	Norway	8	C	?	protogranular	27	725	700–750	---	---	---	---	---
O18C	Norway	8	C	AG	protogranular	37	725	700–750	SIMS	51	---	---	---
PL1	Lunar Crater	11	X	A	mylonitic	45	1250	1200–1300	SIMS	20	---	---	---
PL10	Lunar Crater	11	X	E	mylonitic	62	1241	---	---	---	---	---	---
PL11	Lunar Crater	11	X	E	mylonitic	62	1250	1200–1300	SIMS	45	---	---	---
PL13	Lunar Crater	11	X	E	porphyroclastic	25	1201	---	SIMS	21	6	57	---
PL6	Lunar Crater	11	X	C	mylonitic	45	1250	1200–1300	SIMS	24	---	---	---
RCiV8-1	Cima	15	X	E	porphyroclastic	16	1006	---	FTIR	---	18	80	261
RCiV8-22	Cima	15	X	A	protogranular	17	1004	---	SIMS	---	8	---	120
RCiV8-6	Cima	15	X	A	granular	15	1013	---	SIMS	---	10	131	140
RDH11	Dish Hill	14	X	A	granular	16	992	---	---	---	---	---	---
RDH14	Dish Hill	14	X	A	granular	11	1072	---	FTIR	---	13	169	183
RDH15	Dish Hill	14	X	E	mylonitic	24	897	---	SIMS	---	---	57	145
RDH23	Dish Hill	14	X	E	mylonitic	19	955	---	SIMS	---	17	---	238
RDH26	Dish Hill	14	X	A	porphyroclastic	16	997	---	FTIR	---	13	133	150
RDH33	Dish Hill	14	X	D	porphyroclastic	24	865	---	FTIR	---	9	84	---
RDH44	Dish Hill	14	X	?	protogranular	21	1000	900–1100	---	---	---	---	---
RDH49	Dish Hill	14	X	E	porphyroclastic	20	991	---	---	---	---	---	---
RNF7	Newfoundland	51	O	A	mylonitic	---	1075	1050–1100	SIMS	81	23	209	---
RNF8	Newfoundland	51	O	?	mylonitic	---	1075	1050–1100	SIMS	57	---	---	---
SQ1	San Quintin	7	X	D	porphyroclastic	36	875	800–950	SIMS	13	19	175	---
SQ2	San Quintin	7	X	D	porphyroclastic	27	875	800–950	SIMS	-1	27	270	339
SQ3	San Quintin	7	X	D	mylonitic	23	875	800–950	SIMS	21	20	182	288
SQ5	San Quintin	7	X	?	porphyroclastic	32	875	800–950	SIMS	11	---	---	---
V17A	Norway	41	C	?	porphyroclastic	70	725	700–750	---	---	---	---	---
V24A	Norway	41	C	B	porphyroclastic	24	725	700–750	SIMS	57	---	---	---
WCiVb36	Cima	15	X	C	porphyroclastic	---	---	---	---	---	---	---	---
WCiVb46	Cima	15	X	E	porphyroclastic	24	970	---	FTIR	---	10	95	128
WCiVb47	Cima	15	X	A	protogranular	24	992	---	FTIR	---	26	239	---
Y12B	Norway	41	C	?	protogranular	42	725	700–750	SIMS	87	---	---	---
YF12	Lunar Crater	11	X	E	mylonitic	53	1258	---	SIMS	4	10	---	147
YF3	Lunar Crater	11	X	E	mylonitic	53	1250	1200–1300	SIMS	5	---	---	---
YF4	Lunar Crater	11	X	?	mylonitic	---	---	---	---	---	---	---	---
YF9a	Lunar Crater	11	X	E	protogranular	49	1219	---	SIMS	15	9	106	77
YFN11	Lunar Crater	11	X	?	mylonitic	67	1219	---	SIMS	5	4	34	---
YFN13	Lunar Crater	11	X	E	porphyroclastic	52	1257	---	SIMS	15	8	82	92

* Peridotite type: X=xenolith; C=continental; O=ophiolite

✣ "?" indicates LPO type was inconclusive from EBSD

† Stress estimated from paleopiezometer of Van der Wal et al. (1993)

‡ T range included if exact T is unknown for given sample. For these samples, T used in plots is based on median value within this range. Exact sample T values for Elephant Butte and Cerro Chato samples come from Byerly and Lassiter (2012); Dish Hill and Cima samples from Bernard and Behr (2017). Regional T ranges for samples from other localities come from studies cited in Supplementary Material.

▼ SIMS analyses from this study; FTIR analyses from Bernard and Behr, 2017

▲ multiply by 16 to convert to ppm H/Si

△ if sample has both opx and cpx water contents, this number is an average of the two calculated olivine contents based on partition coefficients for each phase. Otherwise, if this sample only has water contents for one pyroxene, this number is calculated from that.

678 **Table 2.** Properties of analysed samples

	EBSD-derived values				CT-derived values✦		Modal percentages (of mapped area) ✧					Aspect Ratios §			
Sample Name	**M-index**	**J-index**	**BA-index**	**FIA-index**	***T***	***P'***	**olivine**	**opx**	**cpx**	**spinel**	**other**	**X/Z**	**X/Y**	**Y/Z**	**Flinn constant, *k***
07EB4-1	0.11	3.71	0.52	55.11	0.27	1.23	65	13	20	2	0	---	---	---	---
114027-10	0.18	3.87	0.41	105.53	---	---	74	18	8	1	0	2.73	2.06	1.33	3.23
114027-16	0.13	3.24	0.54	33.12	---	---	74	15	10	1	0	2.01	0.93	2.16	-0.06
114027-23	0.11	3.00	0.48	45.72	---	---	64	17	16	2	0	3.03	2.09	1.45	2.44
114027-6	0.17	4.61	0.63	51.44	---	---	82	16	2	0	0	1.72	0.64	2.69	-0.21
116610-26	0.11	2.71	0.71	77.11	---	---	66	16	18	0	0	---	---	---	---
117200-205	0.12	2.72	0.30	8.63	---	---	66	19	15	0	0	2.90	1.22	2.38	0.16
117200-211	0.22	4.62	0.09	-1.76	0.33	1.43	54	33	12	2	0	---	---	---	---
BELB9-6a	0.16	3.42	0.51	77.19	0.36	1.51	71	16	12	1	0	---	---	---	---
CC07-1-22	0.04	1.67	0.57	173.00	0.08	1.20	77	12	10	1	0	---	---	---	---
CC07-2-1	0.05	2.28	0.37	109.25	0.05	1.21	79	7	14	1	0	---	---	---	---
CG07-1-26	0.02	2.20	0.57	-9.26	---	---	74	13	12	0	0	---	---	---	---
CG07-1-36	0.08	2.10	0.42	-24.14	0.76	1.34	71	15	13	1	0	---	---	---	---
CG07-1-52	0.06	2.34	0.36	41.16	-0.34	1.16	71	15	12	2	0	---	---	---	---
DW8	0.23	5.54	0.47	37.46	0.62	1.36	91	6	3	0	0	2.52	0.94	2.69	-0.04
I7	0.05	2.14	0.26	-28.35	0.33	1.32	78	6	16	0	0	2.17	1.25	1.74	0.34
I8	0.04	1.70	0.63	120.23	0.22	1.30	69	14	17	0	0	2.03	1.98	1.03	38.43
Kb	0.12	2.72	0.47	-15.80	0.41	1.39	67	15	14	3	0	1.56	0.71	2.20	-0.24
KH1	0.14	2.64	0.31	2.18	0.49	1.48	57	21	20	2	0	2.42	0.87	2.78	-0.07
KH2	0.08	2.23	0.13	-6.19	-0.32	1.18	45	21	32	2	0	2.13	0.94	2.26	-0.04
Ki-5-319	0.08	2.60	0.44	56.06	---	---	72	10	17	0	0	---	---	---	---
N117	0.22	5.07	0.24	11.54	-0.24	1.86	85	7	7	0	1	2.60	1.09	2.39	0.06
N122	0.23	5.52	0.52	51.24	0.19	1.48	75	17	6	1	2	2.23	0.98	2.28	-0.02
N167	0.20	4.32	0.09	10.58	---	---	88	7	5	0	0	2.30	1.71	1.35	2.03
N178	0.29	6.49	0.16	-16.03	0.37	1.42	95	2	2	0	1	---	---	---	---
N188	0.17	4.55	0.85	93.58	0.77	1.40	68	23	8	0	0	---	---	---	---
O16D	0.01	1.19	0.10	9.03	0.69	2.43	93	1	1	0	5	3.08	2.46	1.25	5.79
O16E	0.04	1.45	0.36	43.44	0.47	2.24	91	2	1	0	6	2.31	1.17	1.97	0.17
O18A	0.18	3.53	0.47	44.01	---	---	100	0	0	0	0	---	---	---	---
O18B	0.01	1.35	0.68	-61.36	-0.25	1.24	98	0	2	0	0	---	---	---	---
O18C	0.05	1.55	0.33	25.83	-0.87	1.35	99	0	0	1	0	1.72	0.84	2.05	-0.15
PL1	0.22	5.88	0.44	54.25	---	---	99	0	1	0	0	---	---	---	---
PL10	0.09	3.02	0.82	89.61	---	---	86	12	2	0	0	---	---	---	---
PL11	0.37	17.38	0.00	179.20	---	---	---	---	---	---	---	---	---	---	---
PL13	0.31	5.98	0.74	100.88	---	---	82	17	1	0	0	---	---	---	---
PL6	0.23	7.93	0.20	149.52	---	---	---	---	---	---	---	---	---	---	---
RCiV8-1	0.01	1.55	0.57	92.23	-0.37	1.36	59	25	16	1	0	3.06	2.13	1.44	2.58
RCiV8-22	0.11	3.07	0.53	84.30	---	---	77	7	14	2	0	---	---	---	---
RCiV8-6	0.21	3.91	0.47	32.46	-0.10	1.26	68	16	14	2	0	---	---	---	---
RDH11	0.10	2.98	0.63	80.35	0.21	1.32	79	11	9	2	0	---	---	---	---
RDH14	0.13	4.34	0.72	-34.90	---	---	59	31	8	1	0	---	---	---	---
RDH15	0.06	2.54	0.42	103.02	---	---	57	27	15	0	0	3.02	1.59	1.90	0.65
RDH23	0.13	3.46	0.58	105.30	-0.08	1.50	64	15	21	0	0	3.56	1.65	2.17	0.55
RDH26	0.05	2.46	0.36	54.81	0.10	1.44	64	14	21	1	0	3.05	1.77	1.72	1.07
RDH33	0.08	2.31	0.59	82.92	-0.30	1.44	80	15	5	0	0	3.32	1.51	2.20	0.42
RDH44	0.04	3.55	0.36	131.10	-0.34	1.40	49	27	23	1	0	3.44	2.45	1.40	3.62
RDH49	0.03	2.19	0.39	87.89	-0.54	1.31	60	22	17	1	0	3.33	2.19	1.52	2.30
RNF7	0.08	2.35	0.44	64.61	0.59	1.28	49	42	7	1	1	---	---	---	---
RNF8	0.06	2.20	0.30	123.21	0.25	1.26	70	21	4	4	1	---	---	---	---
SQ1	0.09	2.07	0.85	94.26	0.09	1.45	89	7	4	0	0	2.65	1.30	2.03	0.30
SQ2	0.11	2.42	0.51	125.89	0.51	1.25	66	18	14	2	0	2.49	1.12	2.22	0.10
SQ3	0.08	2.95	0.68	114.30	---	---	61	21	18	0	0	4.75	2.36	2.01	1.35
SQ5	0.11	2.32	0.69	-46.77	---	---	82	12	5	1	0	---	---	---	---
V17A	0.03	1.45	0.41	81.74	0.69	1.69	87	5	8	0	0	1.85	1.07	1.72	0.10
V24A	0.03	1.35	0.53	59.14	0.19	2.85	90	0	0	0	10	2.02	0.95	2.11	-0.04
WCiVb36	0.10	3.44	0.36	179.20	0.30	1.63	28	0	18	0	54	2.45	1.09	2.25	0.07
WCiVb46	0.08	2.86	0.31	102.00	-0.24	1.47	59	19	21	1	0	3.72	2.52	1.47	3.22
WCiVb47	0.11	3.09	0.57	79.47	-0.20	1.53	67	28	5	0	0	2.67	1.79	1.49	1.61
Y12B	0.04	1.43	0.74	31.59	0.17	2.59	99	0	0	0	0	---	---	---	---
YF12	0.09	3.22	0.58	103.79	---	---	93	0	7	0	0	---	---	---	---
YF3	0.22	9.39	0.52	89.52	-0.22	1.23	100	0	0	0	0	---	---	---	---
YF4	0.29	8.81	0.82	96.57	-0.22	1.18	99	0	0	0	0	3.63	1.34	2.70	0.20
YF9a	0.05	1.99	0.45	109.90	0.46	1.17	77	3	20	0	0	---	---	---	---
YFN11	0.12	3.07	0.49	-62.76	---	---	90	9	1	0	0	3.11	1.07	2.89	0.04
YFN13	0.07	1.93	0.76	119.30	---	---	55	19	25	0	0	2.65	0.79	3.33	-0.09

§ X: lineation within the foliation plane; Y: perpendicular to the lineation within the foliation plane; Z: perpendicular to both the lineation and foliation. X/Y ratio calculated from (X/Y)/(Y/Z). Flinn constant, k, calculated from ((X/Y)-1)/((Y/Z)-1)

✦From SLD method. See supplementary materials for SVD values.

✧ Modal percentages as calculated with MTEX over mapped area. Not necessarily representative of the sample overall

References

Abt, D. L., Fischer, K. M., Abers, G. A., Protti, M., González, V., & Strauch, W. (2010). Constraints on upper mantle anisotropy surrounding the Cocos slab from SK(K)S splitting. *Journal of Geophysical Research: Solid Earth*, *115*, 1–16.

Abt, D. L., Fischer, K. M., Abers, G. A., Strauch, W., Protti, J. M., & González, V. (2009). Shear wave anisotropy beneath Nicaragua and Costa Rica: Implications for flow in the mantle wedge. *Geochemistry, Geophysics, Geosystems*, *10*.

Aubaud, C., Withers, A. C., Hirschmann, M. M., Guan, Y., Leshin, L. A., Mackwell, S. J., & Bell, D. R. (2007). Intercalibration of FTIR and SIMS for hydrogen measurements in glasses and nominally anhydrous minerals. *American Mineralogist*, *92*, 811–828.

Auer, L., Becker, T. W., Boschi, L., & Schmerr, N. (2015). Thermal structure, radial anisotropy, and dynamics of oceanic boundary layers. *Geophysical Research Letters*, *42*, 9740–9749.

Bachmann, F., Hielscher, R., & Schaeben, H. (2010). Texture Analysis with MTEX Free and Open Source Software Toolbox. *Solid State Phenomena*, *160*, 63–68.

Bai, Q., Mackwell, S. J., & Kohlstedt, D. L. (1991). High-temperature creep of olivine single crystals 1. Mechanical results for buffered samples. *Journal of Geophysical Research*, *96*, 2441.

Baptiste, V., Tommasi, A., Vauchez, A., Demouchy, S., & Rudnick, R. L. (2015). Deformation, hydration, and anisotropy of the lithospheric mantle in an active rift: Constraints from mantle xenoliths from the North Tanzanian Divergence of the East African Rift. *Tectonophysics*, *639*, 34–55.

Bascou, J., Delpech, G., Vauchez, A., Moine, B. N., Cottin, J.-Y., & Barruol, G. (2008). An integrated study of microstructural, geochemical, and seismic properties of the lithospheric mantle above the Kerguelen plume (Indian Ocean). *Geochemistry, Geophysics, Geosystems*, *9*.

Becker, T. W., Chevrot, S., Schulte-Pelkum, V., & Blackman, D. K. (2006). Statistical properties of seismic anisotropy predicted by upper mantle geodynamic models. *Journal of Geophysical Research*, *111*, B08309.

Becker, T. W., Kustowski, B., & Ekström, G. (2008). Radial seismic anisotropy as a constraint for upper mantle rheology. *Earth and Planetary Science Letters*, *267*, 213–227.

Behr, W. M., & Smith, D. (2016). Deformation in the mantle wedge associated with Laramide flat-slab subduction. *Geochemistry, Geophysics, Geosystems*, *17*, 2643–2660.

712 Bell, D. R., Ihinger, P. D., & Rossman, G. R. (1995). Quantitative analysis of trace OH in
713 garnet and pyroxenes. *American Mineralogist*, *80*, 465–474.

714 Bell, D. R., Rossman, G. R., Maldener, J., Endisch, D., & Rauch, F. (2003). Hydroxide in
715 olivine: A quantitative determination of the absolute amount and calibration of the IR
716 spectrum. *Journal of Geophysical Research: Solid Earth*, *108*.

717 Bernard, R. E., & Behr, W. M. (2017). Fabric heterogeneity in the Mojave lower crust and
718 lithospheric mantle in Southern California. *Journal of Geophysical Research: Solid Earth*,
719 *122*, 5000–5025.

720 Boneh, Y., Morales, L. F. G., Kaminski, E., & Skemer, P. (2015). Modeling olivine CPO evo-
721 lution with complex deformation histories: Implications for the interpretation of seismic
722 anisotropy in the mantle. *Geochemistry, Geophysics, Geosystems*, *16*, 3436–3455.

723 Boneh, Y., & Skemer, P. (2014). The effect of deformation history on the evolution of olivine
724 CPO. *Earth and Planetary Science Letters*, *406*, 213–222.

725 Boneh, Y., Wallis, D., Hansen, L. N., Krawczynski, M. J., & Skemer, P. (2017). Oriented
726 grain growth and modification of frozen anisotropy' in the lithospheric mantle. *Earth and*
727 *Planetary Science Letters*, *474*, 368–374.

728 Bunge, H.-J. H. J. (1982). *Texture analysis in materials science: Mathematical methods*.
729 London: Butterworths.

730 Bystricky, M., Kunze, K., Burlini, L., & Burg, J. P. (2000). High shear strain of olivine
731 aggregates: Rheological and seismic consequences. *Science*, *290*, 1564–1567.

732 Cao, Y., Jung, H., & Song, S. (2017). Olivine fabrics and tectonic evolution of fore-arc
733 mantles: A natural perspective from the Songshugou dunite and harzburgite in the Qinling
734 orogenic belt, central China. *Geochemistry, Geophysics, Geosystems*, *18*, 907–934.

735 Chatzaras, V., Kruckenberg, S. C., Cohen, S. M., Medaris, L. G., Withers, A. C., & Bagley,
736 B. (2016). Axial-type olivine crystallographic preferred orientations: The effect of strain
737 geometry on mantle texture. *Journal of Geophysical Research: Solid Earth*, *121*, 4895–
738 4922.

739 Chin, E. J., Soustelle, V., Hirth, G., Saal, A. E., Kruckenberg, S. C., & Eiler, J. M. (2016).
740 Microstructural and geochemical constraints on the evolution of deep arc lithosphere.
741 *Geochemistry, Geophysics, Geosystems*, *17*, 2497–2521.

742 Demouchy, S., Jacobsen, S. D., Gaillard, F., & Stern, C. R. (2006). Rapid magma ascent
743 recorded by water diffusion profiles in mantle olivine. *Geology*, *34*, 429.

Drury, M. R., Lallemant, H. G. A., Pennock, G. M., & Palasse, L. N. (2011). Crystal preferred orientation in peridotite ultramylonites deformed by grain size sensitive creep, Etang de Lers, Pyrenees, France. *Journal of Structural Geology*, *33*, 1776–1789.

Durham, W. B., & Goetze, C. (1977). Plastic flow of oriented single crystals of olivine: 1. Mechanical data. *Journal of Geophysical Research*, *82*, 5737–5753.

Dygert, N., Bernard, R. E., & Behr, W. M. (2019). Great Basin mantle xenoliths record active lithospheric downwelling beneath central Nevada. *Geochemistry, Geophysics, Geosystems*, *20*.

Falus, G., Tommasi, A., Ingrin, J., & Szabó, C. (2008). Deformation and seismic anisotropy of the lithospheric mantle in the southeastern Carpathians inferred from the study of mantle xenoliths. *Earth and Planetary Science Letters*, *272*, 50–64.

Flinn, D. (1965). On the Symmetry Principle and the Deformation Ellipsoid. *Geological Magazine*, *102*, 36–45.

Ford, H. A., Long, M. D., & Wirth, E. A. (2016). Midlithospheric discontinuities and complex anisotropic layering in the mantle lithosphere beneath the Wyoming and Superior Provinces. *Journal of Geophysical Research: Solid Earth*, *121*, 6675–6697.

Frese, K., Trommsdorff, V., & Kunze, K. (2003). Olivine [100] normal to foliation: lattice preferred orientation in prograde garnet peridotite formed at high H 2 O activity, Cima di Gagnone (Central Alps). *Contributions to Mineralogy and Petrology*, *145*, 75–86.

Goetze, C. (1978). The Mechanisms of Creep in Olivine. *Philosophical Transactions of the Royal Society A: Mathematical, Physical and Engineering Sciences*, *288*, 99–119.

Hansen, L. N., & Warren, J. M. (2015). Quantifying the effect of pyroxene on deformation of peridotite in a natural shear zone. *Journal of Geophysical Research: Solid Earth*, *120*, 2717–2738.

Hansen, L. N., Warren, J. M., Zimmerman, M. E., & Kohlstedt, D. L. (2016). Viscous anisotropy of textured olivine aggregates, Part 1: Measurement of the magnitude and evolution of anisotropy. *Earth and Planetary Science Letters*, *445*, 92–103.

Hansen, L. N., Zhao, Y.-H., Zimmerman, M. E., & Kohlstedt, D. L. (2014). Protracted fabric evolution in olivine: Implications for the relationship among strain, crystallographic fabric, and seismic anisotropy. *Earth and Planetary Science Letters*, *387*, 157–168.

Hansen, L. N., Zimmerman, M. E., & Kohlstedt, D. L. (2011). Grain boundary sliding in San Carlos olivine: Flow law parameters and crystallographic-preferred orientation. *Journal of Geophysical Research*, *116*, B08201.

Hidas, K., Falus, G., Szabó, C., Szabó, J., Kovács, I., & Földes, T. (2007). Geodynamic implications of flattened tabular equigranular textured peridotites from the Bakony-Balaton Highland Volcanic Field (Western Hungary). *Journal of Geodynamics*, *43*, 484–503.

Hirth, G., & Kohlstedt, D. L. (1996). Water in the oceanic upper mantle: Implications for rheology, melt extraction and the evolution of the lithosphere. *Earth and Planetary Science Letters*, *144*, 93–108.

Hoernle, K., Abt, D. L., Fischer, K. M., Nichols, H., Hauff, F., Abers, G. A., Van Den Bogaard, P., Heydolph, K., Alvarado, G., Protti, M., & Strauch, W. (2008). Arc-parallel flow in the mantle wedge beneath Costa Rica and Nicaragua. *Nature*, *451*, 1094–1097.

Holtzman, B. K., Kohlstedt, D. L., Zimmerman, M. E., Heidelbach, F., Hiraga, T., & Hustoft, J. (2003). Melt segregation and strain partitioning: implications for seismic anisotropy and mantle flow. *Science (New York, N.Y.)*, *301*, 1227–30.

Hossack, J. R. (1968). Pebble deformation and thrusting in the Bygdin area (Southern Norway). *Tectonophysics*, *5*, 315–339.

Ingrin, J., Hercule, S., & Charton, T. (1995). Diffusion of hydrogen in diopside: Results of dehydration experiments. *Journal of Geophysical Research: Solid Earth*, *100*, 15489–15499.

Ismaïl, W. B., & Mainprice, D. (1998). An olivine fabric database: an overview of upper mantle fabrics and seismic anisotropy. *Tectonophysics*, *296*, 145–157.

Jelinek, V. (1981). Characterization of the magnetic fabric of rocks. *Tectonophysics*, *79*, T63–T67.

Jin, Z., Bai, Q., & Kohlstedt, D. (1994). High-temperature creep of olivine crystals from four localities. *Physics of the Earth and Planetary Interiors*, *82*, 55–64.

Jung, H., & Karato, S.-i. (2001). Water-induced fabric transitions in olivine. *Science (New York, N.Y.)*, *293*, 1460–3.

Jung, H., Katayama, I., Jiang, Z., Hiraga, T., & Karato, S. (2006). Effect of water and stress on the lattice-preferred orientation of olivine. *Tectonophysics*, *421*, 1–22.

Jung, H., Lee, J., Ko, B., Jung, S., Park, M., Cao, Y., & Song, S. (2013). Natural type-C olivine fabrics in garnet peridotites in North Qaidam UHP collision belt, NW China. *Tectonophysics*, *594*, 91–102.

Jung, H., Mo, W., & Choi, S. H. (2009a). Deformation microstructures of olivine in peridotite from Spitsbergen, Svalbard and implications for seismic anisotropy. *Journal of Metamorphic Geology*, *27*, 707–720.

Jung, H., Mo, W., & Green, H. W. (2009b). Upper mantle seismic anisotropy resulting from pressure-induced slip transition in olivine. *Nature Geoscience*, *2*, 73–77.

Jung, S., Jung, H., & Austrheim, H. (2014). Characterization of olivine fabrics and mylonite in the presence of fluid and implications for seismic anisotropy and shear localization. *Earth, Planets, and Space*, *66*.

Kaczmarek, M.-A., & Reddy, S. M. (2013). Mantle deformation during rifting: Constraints from quantitative microstructural analysis of olivine from the East African Rift (Marsabit, Kenya). *Tectonophysics*, *608*, 1122–1137.

Kamei, A., Obata, M., Michibayashi, K., Hirajima, T., & Svojtka, M. (2010). Two contrasting fabric patterns of olivine observed in garnet and spinel peridotite from a mantle-derived ultramafic mass enclosed in felsic granulite, the Moldanubian Zone, Czech Republic. *Journal of Petrology*, *51*, 101–123.

Kaminski, É. (2002). The influence of water on the development of lattice preferred orientation in olivine aggregates. *Geophysical Research Letters*, *29*, 1576.

Karato, S. (1989). Grain growth kinetics in olivine aggregates. *Tectonophysics*, *168*, 255–273.

Karato, S. I., Jung, H., Katayama, I., & Skemer, P. (2008). Geodynamic Significance of Seismic Anisotropy of the Upper Mantle: New Insights from Laboratory Studies. *Annual Review of Earth and Planetary Sciences*, *36*, 59–95.

Katayama, I., Jung, H., & Karato, S.-i. (2004). New type of olivine fabric from deformation experiments at modest water content and low stress. *Geology*, *32*, 1045–1048.

Katayama, I., & Karato, S.-i. (2006). Effect of temperature on the B- to C-type olivine fabric transition and implication for flow pattern in subduction zones. *Physics of the Earth and Planetary Interiors*, *157*, 33–45.

Katayama, I., Karato, S.-i., & Brandon, M. (2005). Evidence of high water content in the deep upper mantle inferred from deformation microstructures. *Geology*, *33*, 613.

Katayama, I., Michibayashi, K., Terao, R., Ando, J.-I., & Komiya, T. (2011). Water content of the mantle xenoliths from Kimberley and implications for explaining textural variations in cratonic roots. *Geological Journal*, *46*, 173–182.

Ketcham, R. A., & Ryan, T. M. (2004). Quantification and visualization of anisotropy in trabecular bone. *Journal of Microscopy*, *213*, 158–171.

Kim, D., & Jung, H. (2015). Deformation microstructures of olivine and chlorite in chlorite peridotites from Almklovdalen in the Western Gneiss Region, southwest Norway, and

implications for seismic anisotropy. *International Geology Review*, *57*, 650–668.

Koga, K., Hauri, E., Hirschmann, M., & Bell, D. (2003). Hydrogen concentration analyses using SIMS and FTIR: Comparison and calibration for nominally anhydrous minerals. *Geochemistry, Geophysics, Geosystems*, *4*.

Kohlstedt, D. L., Keppler, H., & Rubie, D. C. (1996). Solubility of water in the α, β and γ phases of (Mg,Fe) 2 SiO 4. *Contributions to Mineralogy and Petrology*, *123*, 345–357.

Lee, J., & Jung, H. (2015). Lattice-preferred orientation of olivine found in diamond-bearing garnet peridotites in Finsch, South Africa and implications for seismic anisotropy. *Journal of Structural Geology*, *70*, 12–22.

Lister, G., & Hobbs, B. (1980). The simulation of fabric development during plastic deformation and its application to quartzite: the influence of deformation history. *Journal of Structural Geology*, *2*, 355–370.

Llana-Fúnez, S., & Rutter, E. H. (2014). Effect of strain geometry on the petrophysical properties of plastically deformed aggregates: experiments on Solnhofen limestone. *Geological Society, London, Special Publications*, *394*, 167–187.

Lloyd, G. E., Butler, R. W. H., Casey, M., Tatham, D. J., & Mainprice, D. (2011). Constraints on the seismic properties of the middle and lower continental crust. *Geological Society, London, Special Publications*, *360*, 7–32.

Long, M. D. (2013). Constraints on Subduction Geodynamics from Seismic Anisotropy. *Reviews of Geophysics*, *51*, 76–112.

Long, M. D., & Becker, T. W. (2010). Mantle dynamics and seismic anisotropy. *Earth and Planetary Science Letters*, *297*, 341–354.

Long, M. D., Biryol, C. B., Eaken, C. M., Beck, S. L., Wagner, L. S., Zandt, G., Minaya, E., & Tavera, H. (2015). Geochemistry, Geophysics, Geosystems. *Geochemistry Geophysics Geosystems*, *17*.

Mackwell, S. J., Kohlstedt, D. L., & Paterson, M. S. (1985). The role of water in the deformation of olivine single crystals. *Journal of Geophysical Research*, *90*, 11319.

Mainprice, D., Bachmann, F., Hielscher, R., & Schaeben, H. (2015). Descriptive tools for the analysis of texture projects with large datasets using MTEX: strength, symmetry and components. In D. R. Faulkner, E. Mariani, & J. Mecklenburgh (Eds.), *Rock Deformation from Field, Experiments and Theory: A Volume in Honour of Ernie Rutter, Special Publications, 409* (pp. 251–271). Geological Society.

Marshall, E. W., Lassiter, J. C., & Barnes, J. D. (2018). On the (mis)behavior of water in the mantle: Controls on nominally anhydrous mineral water content in mantle peridotites. *Earth and Planetary Science Letters*, *499*, 219–229.

Mehl, L., Hacker, B. R., Hirth, G., & Kelemen, P. B. (2003). Arc-parallel flow within the mantle wedge: Evidence from the accreted Talkeetna arc, south central Alaska. *Journal of Geophysical Research*, *108*, 2375.

Michibayashi, K., Kusafuka, Y., Satsukawa, T., & Nasir, S. J. (2012). Seismic properties of peridotite xenoliths as a clue to imaging the lithospheric mantle beneath NE Tasmania, Australia. *Tectonophysics*, *522*, 218–223.

Michibayashi, K., Mainprice, D., Fujii, A., Uehara, S., Shinkai, Y., Kondo, Y., Ohara, Y., Ishii, T., Fryer, P., Bloomer, S. H., Ishiwatari, A., Hawkins, J. W., & Ji, S. (2016). Natural olivine crystal-fabrics in the western Pacific convergence region: A new method to identify fabric type. *Earth and Planetary Science Letters*, *443*, 70–80.

Michibayashi, K., & Oohara, T. (2013). Olivine fabric evolution in a hydrated ductile shear zone at the Moho Transition Zone, Oman Ophiolite. *Earth and Planetary Science Letters*, *377*, 299–310.

Michibayashi, K., Tasaka, M., Ohara, Y., Ishii, T., Okamoto, A., & Fryer, P. (2007). Variable microstructure of peridotite samples from the southern Mariana Trench: Evidence of a complex tectonic evolution. *Tectonophysics*, *444*, 111–118.

Miyazaki, T., Sueyoshi, K., & Hiraga, T. (2013). Olivine crystals align during diffusion creep of Earth's upper mantle. *Nature*, *502*, 321–326.

Mizukami, T., & Wallis, S. R. (2005). Structural and petrological constraints on the tectonic evolution of the garnet-lherzolite facies Higashi-akaishi peridotite body, Sanbagawa belt, SW Japan. *Tectonics*, *24*.

Mizukami, T., Wallis, S. R., & Yamamoto, J. (2004). Natural examples of olivine lattice preferred orientation patterns with a flow-normal a-axis maximum. *Nature*, *427*, 432.

Morales, L. F. G., & Tommasi, A. (2011). Composition, textures, seismic and thermal anisotropies of xenoliths from a thin and hot lithospheric mantle (Summit Lake, southern Canadian Cordillera). *Tectonophysics*, *507*, 1–15.

Mosenfelder, J. L., Le Voyer, M., Rossman, G. R., Guan, Y., Bell, D. R., Asimow, P. D., & Eiler, J. M. (2011). Analysis of hydrogen in olivine by SIMS: Evaluation of standards and protocol. *American Mineralogist*, *96*, 1725–1741.

Mosenfelder, J. L., & Rossman, G. R. (2013a). Analysis of hydrogen and fluorine in pyroxenes: I. Orthopyroxene. *American Mineralogist*, *98*, 1026–1041.

Mosenfelder, J. L., & Rossman, G. R. (2013b). Analysis of hydrogen and fluorine in pyroxenes: II. Clinopyroxene. *American Mineralogist*, *98*, 1042–1054.

Nagaya, T., Wallis, S. R., Kobayashi, H., Michibayashi, K., Mizukami, T., Seto, Y., Miyake, A., & Matsumoto, M. (2014). Dehydration breakdown of antigorite and the formation of B-type olivine CPO. *Earth and Planetary Science Letters*, *387*, 67–76.

Nicolas, A., Boudier, F., & Boullier, A. M. (1973). Mechanisms of flow in naturally and experimentally deformed peridotites. *American Journal of Science*, *273*, 853–876.

Nicolas, A., & Christensen, N. I. (1987). Formation of anisotropy in upper mantle peridotites: A review. In *Composition, structure and dynamics of the lithosphereasthenosphere system* (pp. 111–123). American Geophysical Union (AGU).

Ohuchi, T., Kawazoe, T., Nishihara, Y., & Irifune, T. (2012). Change of olivine a-axis alignment induced by water: Origin of seismic anisotropy in subduction zones. *Earth and Planetary Science Letters*, *317-318*, 111–119.

Palasse, L., Vissers, R., Paulssen, H., Basu, A., & Drury, M. (2012). Microstructural and seismic properties of the upper mantle underneath a rifted continental terrane (Baja California): An example of sub-crustal mechanical asthenosphere? *Earth and Planetary Science Letters*, *345-348*, 60–71.

Park, M., Jung, H., & Kil, Y. (2014). Petrofabrics of olivine in a rift axis and rift shoulder and their implications for seismic anisotropy beneath the Rio Grande rift. *Island Arc*, *23*, 299–311.

Park, Y., & Jung, H. (2015). Deformation microstructures of olivine and pyroxene in mantle xenoliths in Shanwang, eastern China, near the convergent plate margin, and implications for seismic anisotropy. *International Geology Review*, *57*, 629–649.

Paterson, M. S. (1982). The determination of hydroxyl by infrared absorption in quartz, silicate glasses and similar materials. *Bull Mineral.*, *105*, 20–29.

Pera, E., Mainprice, D., & Burlini, L. (2003). Anisotropic seismic properties of the upper mantle beneath the Torre Alfina area (Northern Apennines, Central Italy). *Tectonophysics*, *370*, 11–30.

Peslier, A. H., & Luhr, J. F. (2006). Hydrogen loss from olivines in mantle xenoliths from Simcoe (USA) and Mexico: mafic alkalic magma ascent rates and water budget of the sub-continental lithosphere. *Earth and Planetary Science Letters*, *242*, 302–319.

Précigout, J., & Hirth, G. (2014). B-type olivine fabric induced by grain boundary sliding. *Earth and Planetary Science Letters*, *395*, 231–240.

Qi, C., Hansen, L. N., Wallis, D., Holtzman, B. K., & Kohlstedt, D. L. (2018). Crystallographic Preferred Orientation of Olivine in Sheared Partially Molten Rocks: The Source of the a-c Switch. *Geochemistry, Geophysics, Geosystems*, *19*, 316–336.

Raterron, P., Amiguet, E., Chen, J., Li, L., & Cordier, P. (2009). Experimental deformation of olivine single crystals at mantle pressures and temperatures. *Physics of the Earth and Planetary Interiors*, *172*, 74–83.

Ribe, N. M., & Yu, Y. (1991). A theory for plastic deformation and textural evolution of olivine polycrystals. *Journal of Geophysical Research*, *96*, 8325.

Satsukawa, T., & Michibayashi, K. (2014). Flow in the uppermost mantle during back-arc spreading revealed by Ichinomegata peridotite xenoliths, NE Japan. *Lithos*, *189*, 89–104.

Satsukawa, T., Michibayashi, K., Raye, U., Anthony, E. Y., Pulliam, J., & Stern, R. (2010). Uppermost mantle anisotropy beneath the southern Laurentian margin: Evidence from Knippa peridotite xenoliths, Texas. *Geophysical Research Letters*, *37*.

Skemer, P., & Hansen, L. N. (2016). Inferring upper-mantle flow from seismic anisotropy: An experimental perspective. *Tectonophysics*, *668-669*, 1–14.

Skemer, P., Katayama, I., Jiang, Z., & Karato, S.-I. (2005). The misorientation index: Development of a new method for calculating the strength of lattice-preferred orientation. *Tectonophysics*, *411*, 157–167.

Skemer, P., Katayama, I., & Karato, S.-i. (2006). Deformation fabrics of the Cima di Gagnone peridotite massif, Central Alps, Switzerland: evidence of deformation at low temperatures in the presence of water. *Contributions to Mineralogy and Petrology*, *152*, 43–51.

Skemer, P., Sundberg, M., Hirth, G., & Cooper, R. (2011). Torsion experiments on coarse-grained dunite: implications for microstructural evolution when diffusion creep is suppressed. *Geological Society, London, Special Publications*, *360*, 211–223.

Skemer, P., Warren, J. M., Hansen, L. N., Hirth, G., & Kelemen, P. B. (2013). The influence of water and LPO on the initiation and evolution of mantle shear zones. *Earth and Planetary Science Letters*, *375*, 222–233.

Skemer, P., Warren, J. M., & Hirth, G. (2012). The influence of deformation history on the interpretation of seismic anisotropy. *Geochemistry, Geophysics, Geosystems*, *13*, n/a–n/a.

Skemer, P., Warren, J. M., Kelemen, P. B., & Hirth, G. (2010). Microstructural and Rheological Evolution of a Mantle Shear Zone. *Journal of Petrology*, *51*, 43–53.

Smith, C. S. (1948). Grains, phases, and interfaces: An introduction of microstructure. *Trans. Metall. Soc. AIME*, *175*, 15–51.

Soustelle, V., Tommasi, A., Demouchy, S., & Ionov, D. A. (2010). Deformation and Fluid-Rock Interaction in the Supra-subduction Mantle: Microstructures and Water Contents in Peridotite Xenoliths from the Avacha Volcano, Kamchatka. *Journal of Petrology*, *51*, 363–394.

Sundberg, M., & Cooper, R. F. (2008). Crystallographic preferred orientation produced by diffusional creep of harzburgite: Effects of chemical interactions among phases during plastic flow. *Journal of Geophysical Research*, *113*, B12208.

Tasaka, M., Michibayashi, K., & Mainprice, D. (2008). B-type olivine fabrics developed in the fore-arc side of the mantle wedge along a subducting slab. *Earth and Planetary Science Letters*, *272*, 747–757.

Tommasi, A., Godard, M., Coromina, G., Dautria, J.-M., & Barsczus, H. (2004). Seismic anisotropy and compositionally induced velocity anomalies in the lithosphere above mantle plumes: a petrological and microstructural study of mantle xenoliths from French Polynesia. *Earth and Planetary Science Letters*, *227*, 539–556.

Tommasi, A., Mainprice, D., Canova, G., & Chastel, Y. (2000). Viscoplastic self-consistent and equilibrium-based modeling of olivine lattice preferred orientations: Implications for the upper mantle seismic anisotropy. *Journal of Geophysical Research: Solid Earth*, *105*, 7893–7908.

Tommasi, A., Tikoff, B., & Vauchez, A. (1999). Upper mantle tectonics: three-dimensional deformation, olivine crystallographic fabrics and seismic properties. *Earth and Planetary Science Letters*, *168*, 173–186.

Tommasi, A., Vauchez, A., Godard, M., & Belley, F. (2006). Deformation and melt transport in a highly depleted peridotite massif from the Canadian Cordillera: Implications to seismic anisotropy above subduction zones. *Earth and Planetary Science Letters*, *252*, 245–259.

Van der Wal, D., Chopra, P., Drury, M., & Gerald, J. F. (1993). Relationships between dynamically recrystallized grain size and deformation conditions in experimentally deformed olivine rocks. *Geophysical Research Letters*, *20*, 1479–1482.

1004 Vauchez, A., Dineur, F., & Rudnick, R. (2005). Microstructure, texture and seismic
1005 anisotropy of the lithospheric mantle above a mantle plume: Insights from the Labait
1006 volcano xenoliths (Tanzania). *Earth and Planetary Science Letters*, *232*, 295–314.

1007 Wallis, D., Hansen, L., Tasaka, M., Kumamoto, K., Parsons, A., Lloyd, G., Kohlstedt, D.,
1008 & Wilkinson, A. (2019). The impact of water on slip system activity in olivine and the
1009 formation of bimodal crystallographic preferred orientations. *Earth and Planetary Science*
1010 *Letters*, *508*, 51–61.

1011 Wang, L., Miyajima, N., Kawazoe, T., & Katsura, T. (2019). Activation of [100](001) slip
1012 system by water incorporation in olivine and the cause of seismic anisotropy decrease with
1013 depth in the asthenosphere. *American Mineralogist*, *104*, 47–52.

1014 Wang, Q., Xia, Q.-K., O'Reilly, S. Y., Griffin, W. L., Beyer, E. E., & Brueckner, H. K.
1015 (2013a). Pressure- and stress-induced fabric transition in olivine from peridotites in the
1016 Western Gneiss Region (Norway): implications for mantle seismic anisotropy. *Journal of*
1017 *Metamorphic Geology*, *31*, 93–111.

1018 Wang, Y., Zhang, J., & Shi, F. (2013b). The origin and geophysical implications of a
1019 weak C-type olivine fabric in the Xugou ultrahigh pressure garnet peridotite. *Earth and*
1020 *Planetary Science Letters*, *376*, 63–73.

1021 Warren, J. M., & Hauri, E. H. (2014). Pyroxenes as tracers of mantle water variations.
1022 *Journal of Geophysical Research: Solid Earth*, *119*, 1851–1881.

1023 Warren, J. M., Hirth, G., & Kelemen, P. B. (2008). Evolution of olivine lattice preferred
1024 orientation during simple shear in the mantle. *Earth and Planetary Science Letters*, *272*,
1025 501–512.

1026 Webber, C., Newman, J., Holyoke, C. W., Little, T., & Tikoff, B. (2010). Fabric development
1027 in cm-scale shear zones in ultramafic rocks, Red Hills, New Zealand. *Tectonophysics*, *489*,
1028 55–75.

1029 Wenk, H.-R., Bennett, K., Canova, G. R., & Molinari, A. (1991). Modelling plastic defor-
1030 mation of peridotite with the self-consistent theory. *Journal of Geophysical Research*, *96*,
1031 8337.

1032 White, S. (1977). Geological significance of recovery and recrystallization processes in
1033 quartz. *Tectonophysics*, *39*, 143–170.

1034 Wirth, E. A., & Long, M. D. (2014). A contrast in anisotropy across mid-lithospheric
1035 discontinuities beneath the central United StatesA relic of craton formation. *Geology*, *42*,
1036 851–854.

1037 Xu, Z., Wang, Q., Ji, S., Chen, J., Zeng, L., Yang, J., Chen, F., Liang, F., & Wenk, H.-R.
1038 (2006). Petrofabrics and seismic properties of garnet peridotite from the UHP Sulu terrane
1039 (China): Implications for olivine deformation mechanism in a cold and dry subducting
1040 continental slab. *Tectonophysics*, *421*, 111–127.

1041 Yang, K., Hidas, K., Falus, G., Szabó, C., Nam, B., Kovács, I., & Hwang, B. (2010). Relation
1042 between mantle shear zone deformation and metasomatism in spinel peridotite xenoliths
1043 of Jeju Island (South Korea): evidence from olivine CPO and trace elements. *Journal of*
1044 *Geodynamics*, *50*, 424–440.

1045 Yuan, H., & Romanowicz, B. (2010). Lithospheric layering in the North American craton.
1046 *Nature*, *466*, 1063–1068.

1047 Zhang, S., Karato, S.-i., Fitz Gerald, J., Faul, U. H., & Zhou, Y. (2000). Simple shear
1048 deformation of olivine aggregates. *Tectonophysics*, *316*, 133–152.